A MICROFLUIDIC SYSTEM FOR LOCALISED GROWTH OF BIOFILMS AND STUDIES OF REALATED BIOCHEMICAL KINETICS

Mémoire

Nahid Babaei Aznaveh

Maîtrise en chimie
Maître ès sciences (M.Sc.)

Québec, Canada

Résumé

Nous avons développé une biopuce de microfluidique qui est capable de surveiller continuellement la population de cellules dans les biofilms en conditions d'écoulement laminaire bien contrôlées. Ce dispositif microfluidique est capable de modeler la formation des biofilms linéaires en utilisant une approche de flux basé sur un modèle. Les considérations de conception et méthodologie de fabrication d'un micro-bioréacteur à deux niveaux, inclus le flux basé sur un modèle (FT-μBR) qui génère un flux de croissance du biofilm entouré par les 3 côtés par un flux de confinement et inhibiteur de croissance.

Grâce à une combinaison d'expériences et de simulations, nous avons évalué et exploité exhaustivement les paramètres de contrôle pour manipuler les dimensions du modèle de flux de croissance du biofilm. Ce dispositif est ensuite utilisé pour développer des modèles linéaires du biofilm avec des dimensions contrôlables. Une étude de validation de principe utilisant le dispositif démontre son utilité dans la réalisation des mesures de taux de croissance du biofilms dans différents environnements de force de cisaillement. Cela ouvre la voie à des études quantitatives sur les effets de l'environnement des cisaillements locaux sur les propriétés des biofilms et pour la synthèse d'une nouvelle génération de biomatériaux fonctionnels ayant des propriétés contrôlables.

Abstract

We have developed a microfluidic biochip that is capable of continuously monitoring cell population in biofilms under well-controlled laminar flow conditions. This microfluidic device capable of patterning linear biofilm formations using a flow-templating approach. The design considerations and fabrication methodology of a two level flow-templating micro-bioreactor (FT-μBR) generates a biofilm growth stream surrounded on 3 sides by a growth inhibiting confinement stream. Through a combination of experiments and simulations we comprehensively evaluate and exploit control parameters to manipulate the biofilm growth template stream dimensions. The FT-μBR is then used to grow biofilm patterns with controllable dimensions. A proof-of-principle study using the device demonstrates its utility in conducting biofilm growth rate measurements under different shear stress environments. This opens the way for quantitative studies into the effects of the local shear environment on biofilm properties and for the synthesis of a new generation of functional biomaterials with controllable properties.

Table of Contents:

List of Figures:

List of Tables:

List of Equations:

Abbreviations:

ADP	Adenosine diphosphate ADP
ATP	Adenosine triphosphate
arb. units	Arbitrary unit
NAD^+	Nicotinamide adenine dinucleatide
BF	Biofilms
CFU	Colony forming units
Q_C	Confinement flow rate
Q_T	Template flow rate
CLSM	Confocal laser scanning microscopy diameter
D	Diffusion coefficient
D_H	Hydraulic diameter of the microchannel
DOC	Dissolved organic carbon
EPS	Extracellular polymeric matrix
GFP	Green fluorescent protein
in situ	In the place
I_x	Local pixel intensity
$I_{max, min}$	Maximum and minimum pixel intensities
L_M	Length of microfluidic
w_M	Width of microfluidic
h_M	Height of microfluidic
MF	Microfluidic

FT-μBR	Flow-templated micro bioreactor
MFCS	Microbial fuel cells
Pe	Péclet number
PFA	Perfluoroalkoxy
PDMS	Polydimethylsiloxane
Q_{Tot}	Flowrate total
rpm	Revolutions per minute
τ	Shear stress
w_T	Biofilm templating stream width
h_T	Biofilm templating stream height
t_{lp}	Time duration of the lag phase
COMSTAT	Community Statistics software programs
MEMS	Biomedical microelectromechanical systems
AB	Mix of the two solutions A and B

Acknowledgments:

This dissertation would not be accomplished without the advices and supports of people whom I am greatly indebted.

First and foremost, I wish to express my profound gratitude to Prof. Jesse Greener, my supervisor, for giving me this opportunity to work with his group and introducing me to the challenges of modern Microfluidic sciences and for his invaluable guidance and assistance. I am incredibly grateful and appreciative of his incessant kindness, patience and understanding.

I would also like to thank Doctor Gideon Wolfaardt from the department of chemistry and biology at Ryerson University who gave me the opportunity to have collaboration in his lab, and also, a very big thank you to dear Dr. Elanna Bester, who helped me tremendously and kindly during these 2 years.

I am grateful to all the members of the thesis jury committee: Prof. Dominic Larivière and Prof. Freddy Kleitz for reviewing a thesis, and provide positive and beneficial feedback on the thesis.

I would like to sincerely thank to Profs: Michèle Auger, Michel Pézolet and Steve Charette for allowing access to their labs.

I would like to express my sincere appreciation to my family who have been the source of encouragement and inspiration to me throughout my life.

I would like also to thank all my colleagues (Muhammad Safdar, Jean-Nicola Verin, Eya Mejri, Mkaouar Mahdi), who helped me in this project and for their amity and supports which made great memories throughout my M.Sc. program.

Finally, I acknowledge the financial and technical support of the Centre de recherche sur les matériaux avancés (CERMA) and Centre Québécois sur les Matériaux Fonctionnels (CQMF) and Hydro-Québec for technical and financial help.

Foreword and Statement of Authorship

This thesis is written in a manuscript-based format and consists of 3 chapters. The first chapter is a reference to the biocatalytic activity of biofilm, as a valuable resource for alternative energy and water treatment plant to contamination concerns, and an overview of existing methods and their problems, and presented a new method for controlling and planning the biofilm to improve higher efficiency. In the rest of this chapter microfluidic integration benefits with biofilm are mentioned as the best lab-on-chip, to create accurate and stable hydrodynamic properties.

In the second chapter the materials and equipment used in this project, design, fabrication and modification techniques and preparing biological samples are presented, and at the end, techniques and methods for the characterisation and analysis of the results are described.

Chapters three presents experimental results of this project and the other common project with Ryerson University's microbiology department, in the form of submitted articles.

My contribution in first manuscripts (1) was to perform all the experimental work, data collection and analysis, and all the simulation parts in Figures 9, 16, 17, 18 and 19 designed by my dear colleague Mohammad Safdar.

1. N. B. Aznaveh, M. Safdar, G. Wolfaardt, J. Greener, "Micropatterned biofilm formations by laminar flow-templating", *Lab Chip*, **2014**, DOI: 10.1039/C4LC00084F.

In the second following manuscript I helped for some experimental part. The information from this paper are presented in chapters 2, Materials and Methods, Sections 2.2.4; 2.3.2.2; and chapter 3: Results, Section 3.3.1, 3.3.2.

2. Elanna Bester, Gideon M. Wolfaardt, Nahid B. Aznaveh and Jesse Greener, "Biofilms' Role in Planktonic Cell Proliferation", *Int. J. Mol. Sci.* **2013**, 14, 21965-21982.

Nevertheless, this research work includes more results from my works that presented in other manuscripts such as verification biofilm growth on metal surface deposition in order to SERS imaging (3), (4), (5) as follows:

3. François Paquet-Mercier, Nahid Babaei Aznaveh, Muhammad Safdar and Jesse Greener, "A Microfluidic Bioreactor with *in Situ* SERS Imaging for the Study of Controlled Flow Patterns of Biofilm Precursor Materials", *Sensors*, **2013**, 13, 14714-14727;

4. F.Paquet-Mercier, N. Babaei Aznaveh, M. Safdar, J.Greener "Next generation microfluidic reactors for spectroscopic imaging of biomaterials", *Eur Cell Mater*, **2013**, 26, 81.

5. F. Paquet-Mercier, A. Kara, M. Safdar, N.B. Aznaveh, M. Zarabadi, J. Greener, "Development and calibration of a microfluidic biofilm growth cell with flow-templating and multi-modal characterization", IEEE-EMBC, **2014.**

The last part includes a general conclusion on the work performed and recommendations for future works.

Chapter1: Introduction

1.1. Motivation: Biocatalysts for waste water treatment and energy production

Bacterial biofilms in each ecosystem contains adequate nutrients prevail and metabolize easily. This formation and accumulation of bacteria can cause serious problems in industrial and medical water systems and processes. In addition to the costs imposed for removal and cleaning, biofilms can cause loss of energy and obstruction industrial water systems. Biofilms can also cause the spread of pathogens in water distribution systems.

Biofilms are compact, microbial communities which aggregate and attach to surfaces, usually in an aqueous environment. In the vicinity of a surface due to adhesion complex process, they create significant changes in their phenotype, and exhibit different properties such as increased chemical resistance against antimicrobial agents up to 500 times more compared to free floating cells.
Today, instead of spending large sums to remove biofilms, researchers are trying to isolate them and establish efficient removal properties in order to eliminate increased organic contaminants available in the water and wastewater systems.
The bacteria in a biofilm can consume organic molecules (carbon-based nutrients) from the wastewater, providing energy for their metabolism, while at the same time cleaning it. Bacterial-based cleaning is the most economical way of treatment, rather complex process configurations have resulted. On the other hand, due to excessive use of energy and global warming, the need for stable and green energy is stronger than ever. The large amount of organic waste substances in wastewater also represents an important alternative energy source, in the recent years using of microbial fuel cells represent a new approach to wastewater treatment and generate renewable electricity from a vast array of carbon sources of water containing glucose, acetate or lactate.
Our group intends to focus on the use of biofilms, as a class of materials that has the potential for wide ranging applications in areas including energy, catalysis, bio-MEMS, environmental remediation, and industries such as health, food and naval shipping. We aim to control biofilms functionality for specific applications. In particular, our long-term goal is the optimisation of biofilm-

based materials for use in microbial fuel cells. This novel approach to synthesise biofilms has the potential to produce electrical energy from the breakdown of organic materials found in wastewater, without the need for additional catalytic materials.

While great advances have been made in the understanding of biofilms from the perspective of molecular biology in the last 5-10 years, further advances require quantitative characterisation under well-defined physical conditions. This has prompted new creative approaches to characterisation, such as combined use of confocal laser scanning microscopy and fluorescence correlation spectroscopy for the study of growth and diffusion within the biofilm matrix[1] and flexible flow cells for the estimation of biofilm mechanical properties[2]. Nevertheless, there is a need for a versatile platform that enables both simple and quantitative *in situ* measurements of biofilms using standard laboratory equipment, while achieving strict control over the hydrodynamic environment. Optically transparent microfluidic (MF) channels are ideal environments to manipulate and study biofilms because they can achieve excellent control over hydrodynamic, chemical and thermal conditions and are readily examined by regular optical microscopes. In addition, a major practical advantage includes strongly reduced requirements on growth medium volumes. This opens the way for studies that require high fluid velocities and long-duration experiments, without compromise of growth media sterility when filling or replacing reservoirs. The current approach to growing biofilms in MF channels is to inoculate the entire microchannel, thereby exposing bacteria to the all wall surfaces. However, corner effects in rectangular microchannels result in variations in biofilm properties due to large differences between the values of wall shear stresses at the channel corners versus those at straight wall segments. In addition, recent work shows that biofilm overgrowth can strongly affect the free volume in MF channels, resulting in unpredictable changes to the hydrodynamic environment, thereby undermining the major advantage of MFs[3,4]. Factors such as a nutrient source and concentration have only limited impact on biofilm thickness and density, therefore a new approach to localise and limit biofilm growth in the microchannel is required[5].

This work describes the development and demonstrates the functionality of a micro bioreactor that can overcome the problems above by confining biofilm growth to a region of the MF channel that experiences uniform wall shear stress. This could accomplish by generating co-flowing streams with controllable dimensions that geometrically localise biofilm growth on one microchannel wall and prevent growth in microchannel corners. Resulting biofilms are predicted to

have more uniform dimensions, density, and bioactivity compared to those growing in heterogeneous hydrodynamic environments[6]. The flow-templated micro bioreactor (FT-μBR), presented here, brings specific design and operational enhancements over a co-flow device that we recently used for surface enhanced Raman studies of liquid streams[7]. To the best of our knowledge, the FT-μBR enables, for the first time, patterning of biofilms with controllable dimensions on a single microchannel wall. The biofilms were grown on the wall opposite a coverslip sealing layer to enable unobstructed inspection of the entire channel volume, including the cultured biofilms. Quantitative analysis was conducted using a normal bright-field microscope with validation being provided by numerical simulation. In this work, we analysed the flow-template stream width and height to define and comprehensively explore reactor design features and operational control parameters. We used the FT-μBR for a proof-of-principle study of the biofilm growth rate under different shear stress environments. This work demonstrates the utility of liquid-phase biofilm growth templating to enable accurate studies related to growth in different hydrodynamic environments. It also opens the way for optimising biofilm properties for new uses as functional materials.

1.2.From planktonic to sessile bacterial life and finally biofilm formation

Formation of a biofilm begins with the attachment of suspended bacteria (planktonic) to a surface. These first colonizing bacteria adhere to the surface initially through weak and reversible van der Waals forces. If these colonies have the ability of anchoring themselves on the surface, there is a chance for creating the sessile form using cell adhesion structures such as pili[8]. General definition for biofilms is accumulation of cells connected together and encapsulated and embedded in an extracellular polymeric matrix (EPS) on a solid substratum or interface that can be established on all aquatic and industrial surfaces[9, 10, 11.] The EPS, which is comprises approximately 90 percent of the dry mass of biofilm, versus 10 percent of microorganisms, is responsible for providing the conditions to help bacteria adhere to the surface. The biofilm bacteria are non-motile and undergo cell-cell communication via quorum sensing signals and chemical interactions. In addition to providing energy and nutrients, EPS helps aids in biofilm survival in harsh environments due to its protective properties. The EPS has viscoelastic properties that provide mechanical stability via against detachment, drying, antibiotics, ultraviolet radiation and oxidation[10, 11,12]. For example, biofilm bacteria are 500 times more resistant against antimicrobial sub-

stances, enabling cell proliferation under harsh chemical and hydrodynamic conditions compared to their planktonic counterparts[13]. Physiological changes created in bacterial biofilms are responsible for the increased resistance. This mechanism is due to alterations in gene expression leading to a phenotype shift between the planktonic and sessile forms. The sessile forms are more resistant as they produce exopolysaccharide, have different growth characteristics and take up nutrients and drugs differently from their planktonic counterparts[14, 15] thus, biofilms are able to survive in many different environments where free floating bacteria would be eliminated, wherefore bacteria preferentially reside in biofilms.

1.2.1. Structure and composition of biofilms and EPS

Biofilms are complex communities of microorganisms attach on a surface and typically embedded within a self-produced matrix of EPS. The major matrix components are microbial cells, polysaccharides and water up to 97%. (Table 1)[16]. The other constituents of EPS are proteins, nucleic acids, peptidoglycan, and lipids[17]. In the area of contact between bacteria and surface, the flagella, pili and fimbriae as extracellular structures of bacteria can facilitate cell adhesion with the surface and also stabilise the matrix through the production of several different proteins and polysaccharides. The amount of cellular material within a biofilm and structure of the biofilm EPS can vary depending on environmental conditions, which include surrounding biological materials and organisms, hydrodynamic conditions, temperature, and type and quantity of nutrients available to the cell [11, 12].

Table 1 : Range of composition of biofilm matrices[16]

Component	**% of matrix**
Water	Up to 97%
Microbial cells	2-5% (Many species)
Polysaccharids	1-2%(Neutral and polyanionic)
Proteins	<1-2%(Many, including enzymes)
DNA and RNA	<1-2%(From lysed cells)
Ions	?(Bound and free)

1.2.2. The biofilm life cycle

Microscopic analysis has shown that biofilm formation involves five sequential stages (Figure 1)[9,18] Steps 1 and 2 include the initial adhesion when some bacterial cells in an aqueous environment reversibly attach to a surface. Adhesion at this stage is usually nonspecific, via Van der Waals forces, electrostatic or hydrophobic interactions. Steps three and four involve the irreversible adhesion and biofilm development through the cellular accumulation and subsequent growth and leads to maturation of cells and formation of micro-colonies. The fifth and final step includes separation and detachment of cells by diffusion or due to biofilm erosion. These cells are then able to return to the biofilm life cycle [8, 9, 18].

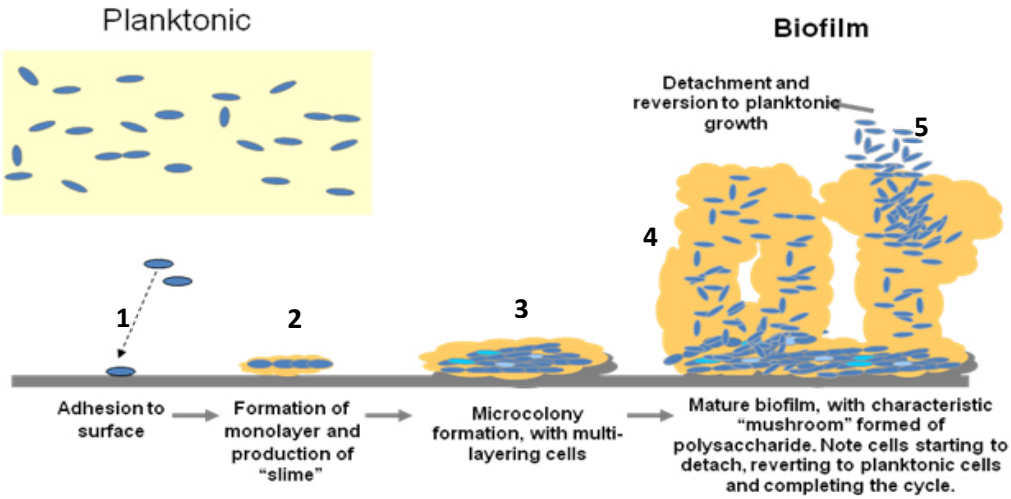

Figure 1: An illustration of the development of the biofilm.[19]

1.2.3. Microbial digestion and metabolism

Bacteria are very small organisms (ca. 1 µm) which can breakdown a huge variety of organic compounds such as glucose and acetate in waste water, into CO_2, protons and electrons[20]. Oxidative phosphorylation is the metabolic pathway in which the mitochondria in cells use their structure, enzymes, and energy released by the oxidation of nutrients to reform adenosine triphosphate (ATP), and the micro-organisms use the produced energy to grow and to maintain their metabolism. During oxidative phosphorylation (Figure 2), microorganisms can release electrons from an electron-rich substrate, using a coenzyme known as nicotinamide adenine dinucleatide or NAD^+ in the low redox potential and transfer these electrons through the electron transport complex by the cell membrane where the final acceptor is reduced. These redox reactions release energy, which is used to form ATP. In eukaryotes, the enzymes in this electron

transport system use the energy released from the oxidation of NADH to pump towards protons across the inner membrane of the mitochondrion. This causes protons to build up in the inter-membrane space, and generate an electrochemical gradient across the membrane which leads to the liberation of energy. Using this energy from a proton gradient, ATP synthase catalyzes the formation of ATP from the phosphorylation of adenosine diphosphate (ADP) with inorganic phosphate, in order to reproduce the energy carrier molecules such as adenosine triphosphate trough the membrane complex[21, 22].

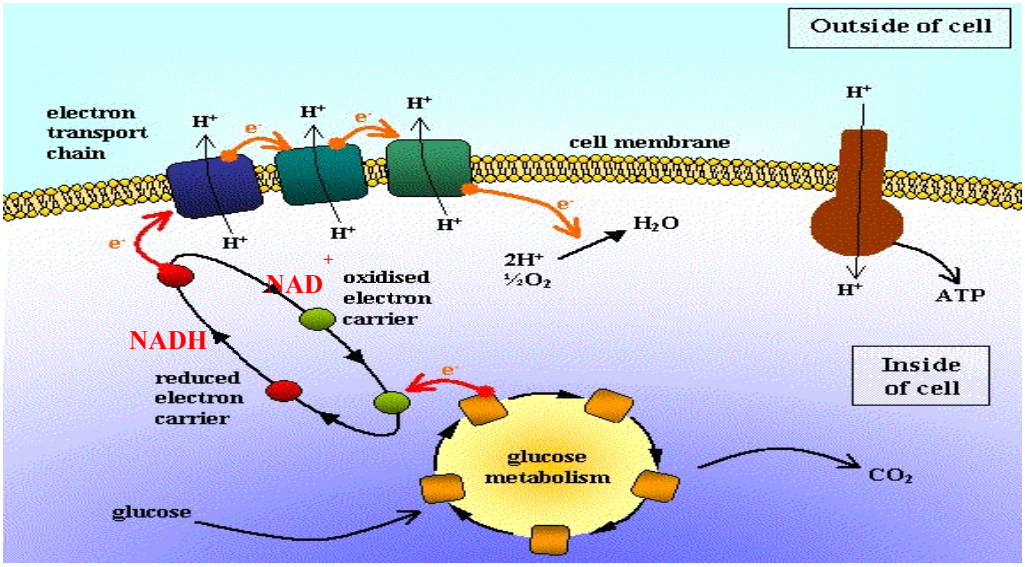

Figure 2 : Glucose metabolism and the electron transport chain of bacteria and mitochondria[23].

Bacteria, for survive and grow in addition to appropriate nutrients, need the presence of a suitable electron acceptor. Depending on the final acceptor, there are two processes for microbial metabolism: Respiration and fermentation.

During respiration, the bacteria grow by using the energy generated by electron transfer to the external electron acceptor. During respiration, microorganisms can release electrons from oxidation (Figure 3) of substrate and transfer these electrons through the electron transport complex by the cell membrane as explained before where the final acceptor that is reduced.

$$\text{Organic waste} + O_2 \xrightarrow[\text{biofilm}]{\text{Seed of}} CO_2 + H_2O$$

Figure 3 : Respiration reaction

1.2.3.1. Microbial digestion of biocatalysts for waste water treatment and energy production

Metabolism of microorganisms in biofilms via oxidation leading to decomposition of organic matter and naturally remove pollutants from the water, are very beneficial. Biofilms have been suggested for industrial application as robust, self-immobilised and self-regenerating catalysts in productive catalysis. They can be an effective and environmentally friendly tool for the industrial production of chemicals. In addition they can catalyze reactions with high specificity under mild condition thereby reducing waste and energy requirement in comparison the chemical process-es[24].

1.2.3.2. Microbial fuel cell

Using biocatalytic agency like the biofilm lead to creating microbial fuel cells as an emerging technology. Microbial fuel cells (MFCs) may become an alternative "green" energy technology of the future as they generate sustainable electricity from biodegradable organic compounds through microbial metabolism. They have the potential to replace traditional fuel cell catalysts, such as Pt, because they are low-maintenance and can operate for long times due their regenera-tive properties. In contrast, Pt is expensive, requires fuel pre-processing to limit poisoning by impurities, and in any case, requires periodic cleaning.

The idea of forming a fuel cell formed based on the similarities of microorganism respiration processes with electrochemical processes that take place in the cell. In the reactor, when bacteria are placed in the anode chamber of a fuel cell that is free of oxygen, they attach to an electrode. Due to lake of oxygen, they must transfer the electrons that they obtain from oxidation of organic substrates (electron donors) somewhere else than to oxygen. They transfer them by microbial extracellular electron transfer in the anode, generating electrons and protons. Then electrons are transferred to the cathode through an external circuit and protons through the internal membrane. At the cathode the electrons, oxygen and protons combine to form only water as (Figure 4)[25, 26].

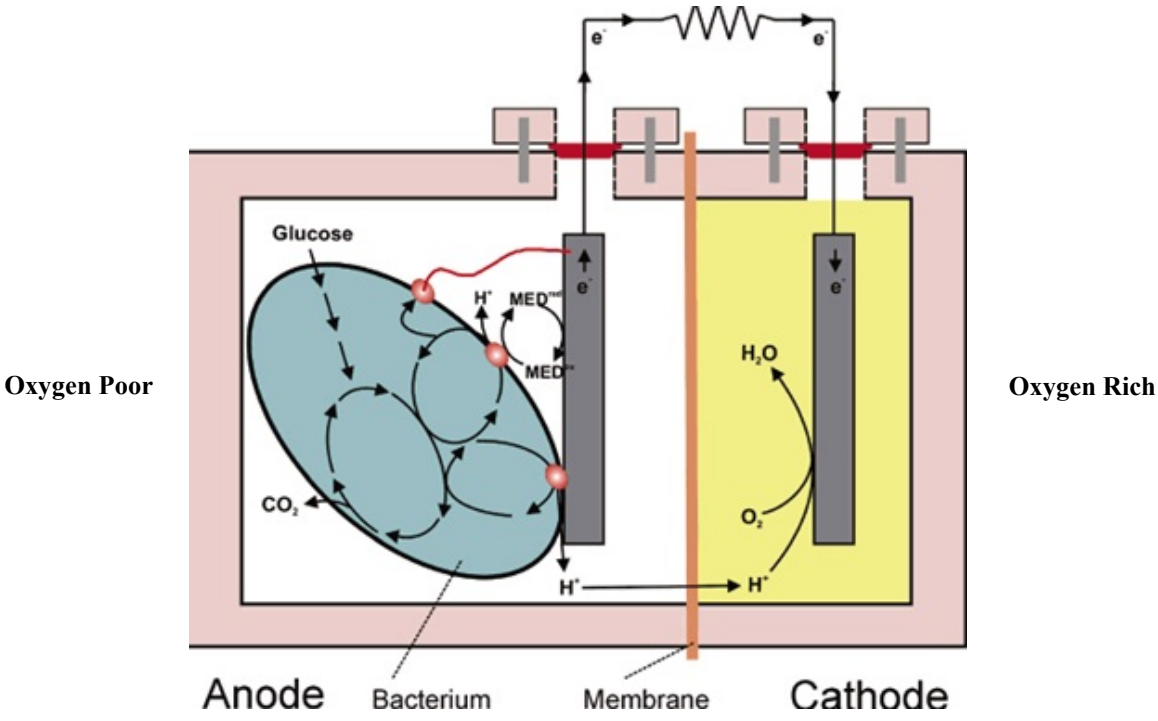

Anode Reaction: **C12H22O11 + 13H2O ---> 12CO2 + 48H+ + 48e-**

Cathode Reaction: $4H^+ + O_2 + 4e^- \rightarrow 2H_2O$

Figure 4 : Microbial fuel cells (MFCs) to turn waste into energy and potable water: under anaerobic conditions, electrons produced by substrate oxidation via bacteria are transferred to anode (negative terminal) and flow to the cathode (positive terminal) linked by a conductive material. For complete the circuit, protons move to cathode compartment through Proton Exchange Membrane[27].

1.3. Benefits of microfluidics in bacterial biofilm studies

Microfluidics is the area of science and technology that is focused on controlling and manipulating simple or complex, mono or multiphase flows in natural or artificial micro systems. At least, one dimension of a microfluidic channel (height or width) should be below 1000 µm (Figure 5)[28, 29].

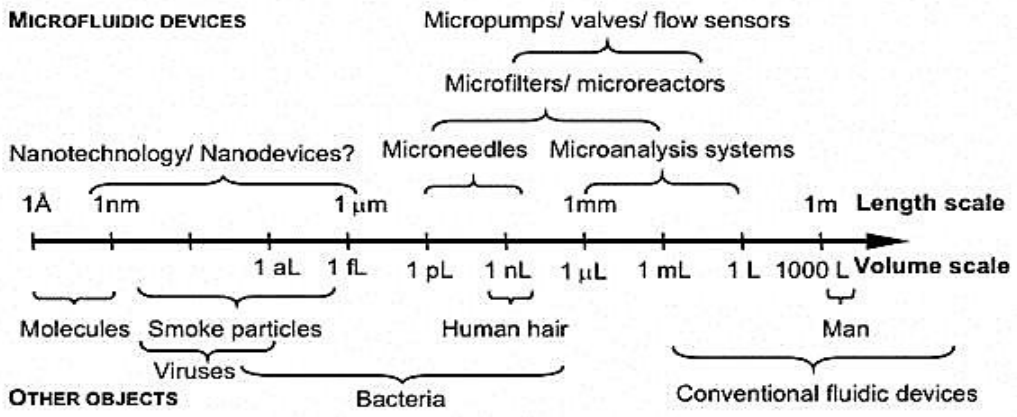

Figure 5 : Size characteristics of microfluidic devices[30].

1.3.1. Low volumes

Microfluidic technology permits the processing, manipulation and miniaturisation of biological experimentation of micro volumes. This technology also allows more accurate, faster and cheaper analysis[31]. In addition, a major practical advantage includes strongly reduced requirements on growth medium volumes during biofilm formation. This opens the way for studies that require high fluid velocities and long-duration experiments, without compromise of growth media sterility when filling or replacing reservoirs[32].

1.3.2. Well defined micro size

Bacterial biofilm growth process usually starts with sticking the bacteria on the surface at the nanometer scale via extracellular mediators such as pili and flagella. The individual cells form microcolonies and then biofilm form with heights in the range between tens and thousands of microns. The micro channels, which are on a compatible size scale, are well-suited for the fundamental studies of growth and biofilm formation[17, 33].

1.3.3. Precise hydrodynamic conditions

The formation, metabolism and immobilised colonies on the surfaces are related very closely with hydrodynamic condition[34]. Due to the surface area to cell volume ratios, we are able to make accurate hydrodynamic conditions and establish a stable temperature profile in the long-

term, thereby giving the ability to control the local microenvironment of microbial cells and biofilms[35]. In this section, two important characteristics of the flow in microchannel, "laminar flow and shear stress", will be explained.

1.3.3.1. Laminar flow:

Laminar flow of liquids that naturally occurs in microchannel is the most important characteristic of microfluidic device which allows parallel flow of two or more different fluids without significant mixing (Figure 6)[36].

The dimensionless Reynolds number (Re) describes whether flow conditions are laminar or turbulent. In microchannels, Re < 2300, indicating laminar flow.

Equation 1 : $Re = \rho v D_H / \mu$

Where ρ is the kinematic density of fluid, v is the mean velocity of fluid, D_H is the hydraulic diameter of the microchannel, and μ is the dynamic viscosity of fluid[37].

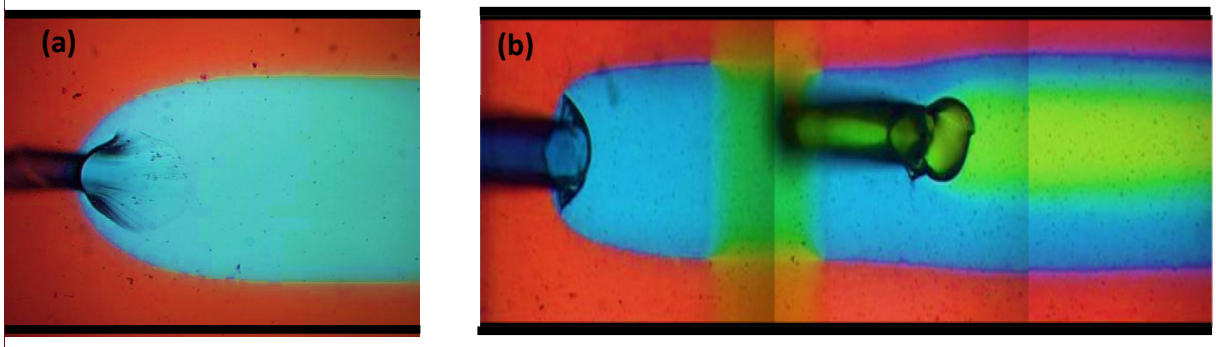

Figure 6 : Optical micrographs of michrochannel include: (a) 2 co-flowing food dye-laden streams (b) 3 co-flowing dyed streams flowing in parallel without mixing.

We will demonstrate how we use the laminar flow conditions to eliminate so-called corner effects (Figure 7) in rectangular microchannels, which can result in variances in biofilm properties.

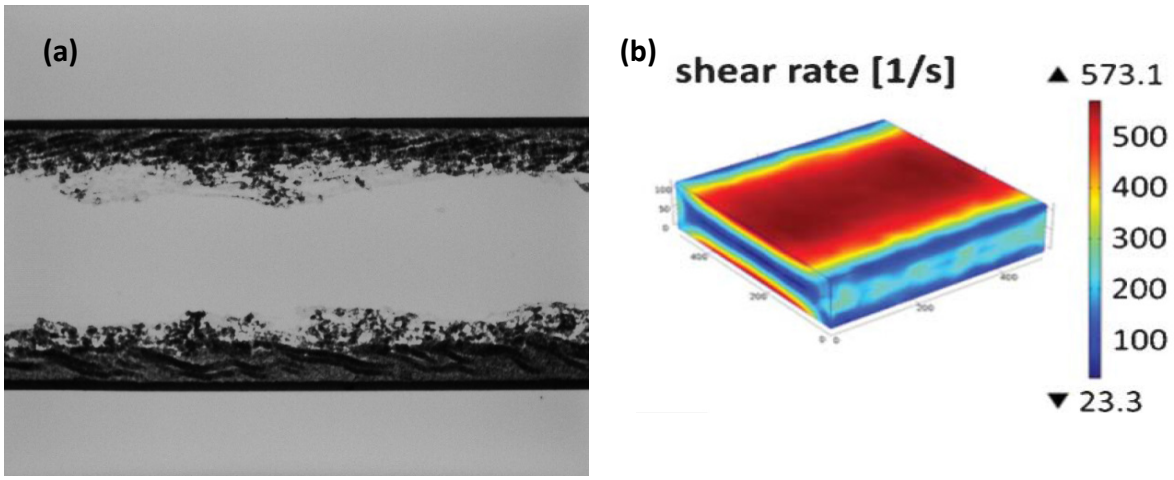

Figure 7 : (a) Optical bright field image of developed biofilm area, showing biofilm growth affected by corner effects via the shear stress near to zero therefore accumulation biofilm in this area. (b) Simulated shear rate distribution in the microfluidic channel that can help for choosing the area with more uniform wall shear stress in order to localised biofilm and eliminate corner effect.

Since in multi- stream laminar flow in the microchannel no convective mixing between the fluids occur, the only remaining mechanism of mixing is diffusion across the mutual liquid–liquid interface between the two streams that acts perpendicular to the flow direction, thus, laminar flow is ideal for carrying controlled substance and confinement of reactants[38]. Diffusion is driven by Brownian motion in which molecules, ions or other small particles spontaneously move over time, from areas of higher to low concentration[39]. The degree of diffusional mixing depends on the diffusivities (D) of the species and the diffusion time according to Equation 2,[40]

Equation 2 **: $D^2 = 2dt$ or $D = \sqrt{2dt}$,**

Where d is the distance a particle that moves in a time (t). Diffusion coefficients are approximately inversely related to molecular size. Generally small molecules have larger D than large molecules[37.]

1.3.3.2. BF response to shear forces

The formation, final structure, morphology, density and metabolism of biofilms have a close relationship with hydrodynamic conditions imposed on it. Specifically, shear force applied to the interface of the biofilm is critical in determining these properties[34] During the initial stages of biofilm growth, the shear stress affects bacterial cell residence time[8]. Shear force can also cause

the detachment of biofilm, which is an important stage of the life cycle[41] that influences the growth, structure, and stability of biofilm[34].

Equation 3 : (Shear stress equation) $\tau_w = 6\mu \times Q/h^2w$

Where Q is the flowrate, τ_w, is the shear stress at the walls, μ the fluid viscosity, w is the channel's width, and h the channel height. Adhesion and detachment of cells depend on the threshold shear stress. Because of the flexibility of matrix, its shape can be changed in response to applied forces. Biofilms grown under higher shear have the thinner and denser structure[42] and stronger adherence and EPS than those grown under low shear[12].

1.3.4. Previous studies using microfluidics for biofilm growth in microfluidic devices

Recently, several manuscripts have been published on the use of microfluidics to control hydrodynamics in low Reynolds number environments while studying its effect on biofilm morphology, mechanical properties, adsorption/detachment, and efficacy of anti-fouling surfaces, streamer formation and planktonic cell proliferation.

Jeongyun Kim and all to investigat the events leading to bacterial attachment to surfaces that influence the biofilm formation and inhibition, preferred to use microfluidic device rather than the conventional methods, such as macro-scale flow cells, because they are low-throughput, require large volumes, and do not allow spatial and temporal control of biofilm community formation[43].

Lukas Richter and all used microfabricated biochips to continuously monitor dynamic responses of cell population to increased shear stress and antimicrobial agent concentration, in a non-invasive manner. Using various bacterial and yeast strains confirmed the high sensitivity of this developed platform for direct identification of microbial strains based on morphological differences and biological composition[44].

Junghyun Kim and all expressed that physical, chemical and biological factors are the most influential factors on the growth, adhesion, proliferation and detachment of biofilms. Microfluidics have been used for analyzing and specifying the effects of factors such as shear stress, surface topography, quorum sensing, signals, temperature, nutrient concentration in a quantitative way,

but characterizing and quantifying the effects the major influencing factors (e.g., shear stress) on bacterial biofilms have not been well studied and underdeveloped.

They investigated the effects of hydrodynamic conditions on biofilm formation by *Pseudomonas aeruginosa* in microfluidic's channels, and found that in addition to the impact of these conditions on the biofilm, biofilm growth on the edge of the channel, causing narrowing of the width of the stream and thus changing the flow velocity. They found that at low Reynolds, increased flow rates increased biofilm growth, the While at higher flow rates with high Reynolds is biofilm Inhibit the growth of the biofilm. These results as a fundamental model can be expanded understanding the relative roles of factors such as shear stress, nutrient requirements, interactions with cells and cell-matrix erosion, and etc. on biofilm formation in microfluidic channels[45].

Microbial fuel cells (MFCs) as explained in Section 1.2.3.2 could be an alternative "green" energy for generating electricity from renewable biodegradable organic compounds through microbial metabolism. Recently miniaturized microbial fuel cell (Figure 8) production has grown, because they have the potential to power small portable electronics with low-cost renewable energy technology. The problem of micro-sized microbial fuel cells is very little ability to generate energy that could be problematic for practical use, so Seokheun Choi attempted to optimise production of biofilm in microfluidic to produce high power density. The progress of this research involves the use of microfluidic device lead to produce, the fewer population of microorganisms and thus allows precise control in microenvironment and hydrodynamic conditions surrounding of the microorganisms. This contributes to a more precise understanding of the mechanisms of extracellular electron transfer in the microorganisms[46].

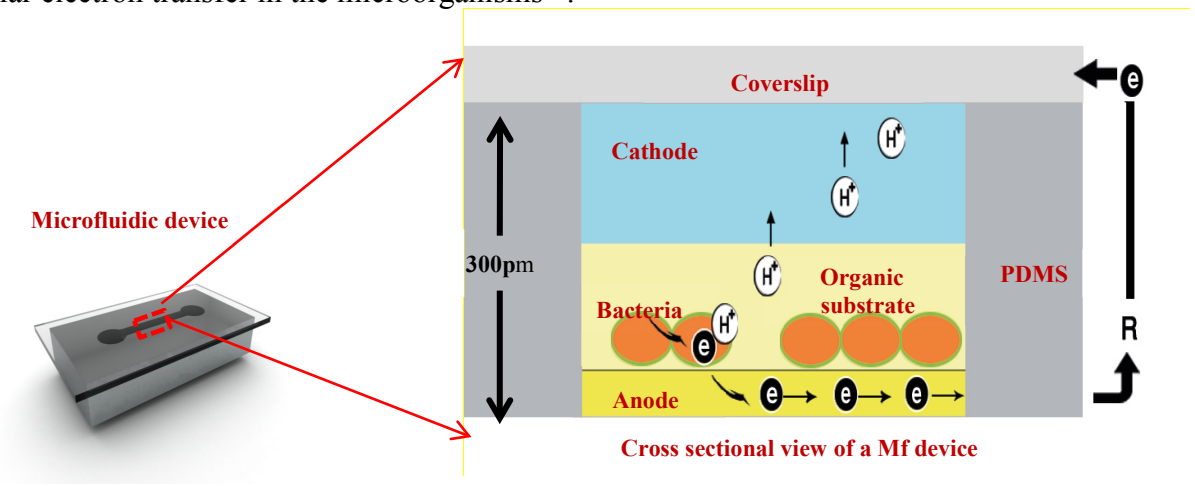

Figure 8: Cross-sectional view of a micro-scale microbial fuel cell (MFC)

Chapter 2: Materials and Methods

2.1. Materials and equipment

This chapter describes the materials and methods used in the present research.

2.1.1. Bacterial strains, culture conditions and characterisation

The gram negative, rod-shaped motile bacterium *Pseudomonas sp*. strain CT07 from (Wolfaardt Lab, Ryerson University) was selected based on its biofilm forming capability for BF formation in the MF platform. We choose *Pseudomonades* because they are benign, have the ability to metabolise a variety of nutrients and form robust biofilms. For example, the strain CT07, which we used in this study, was a benign strain cultured from a cooling tower, while, other strains can cause cystic fibrosis[47].We used a variant that expressed green fluorescent protein (GFP) as a fluorescent protein tag and a non-invasive fluorescent marker. All strains were maintained as glycerol stocks at –80°C. A pre-culture of planktonic *Pseudomonas sp*. was used as inoculum for BF formation. The suspended culture inoculum was obtained by shaking the cultures of planktonic *Pseudomonas sp*. in 3 mL of 5 mM growth media at 300 rpm for 18 h at 30°C.

Routine cultivation of the Pseudomonads was carried out in modified AB defined medium[48] (final concentration of 1.51 mM $(NH_4)_2SO_4$, 3.37 mM Na_2HPO_4, 2.20 mM KH_2PO_4, 179 mM NaCl, 0.1 mM $MgCl_2 \cdot 6H_2O$, 0.01 mM $CaCl_2 \cdot 2H_2O$, and 0.001 mM $FeCl_3$with 10 mM Na-citrate$\cdot 2H_2O$ as the carbon source. Culture ingredients were acquired from Sigma Aldrich and ultrapure water with resistivity of 18.1 $M\Omega \cdot cm^{-1}$ was used in the preparation of all solutions.

2.1.2. Device fabrication materials and equipment

Microfluidic device fabrication materials included polydimethylsiloxane (PDMS) (sylgard184, Dow corning, Canada) and glass cover slips (VWR, Mississauga, Canada). We used PDMS elastomer because it is suitable for various miniaturised bioassays and is easy to work with. It is impermeable to water, nontoxic to cells and permeable to gas, as opposed to silicon and glass[49]. PDMS has the ability to irreversibly bond with glass, silicon, and itself after exposure to oxygen plasma due to the addition of reactive oxygen groups at the surface. Oxygen plasma exposure

causes temporary change to the surface to hydrophilic, which reverts back to hydrophobic due to the mobility of the elastomeric chains.Transparency of this material allows optical imaging with the high penetration depth, due to the short time exposed to oxygen plasma could be converted to a hydrophilic surface[50].

The MF channel features were fabricated by curing the uncrosslinked PDMS polymer against a silicon master mould (FlowJEM Inc., Toronto, Canada). Each level was fabricated separately before they were aligned and bonded. Bonding was achieved by exposing bonding surfaces to air plasma (PCD-001 Harrick Plasma, Ithaca, USA).

2.1.3. Fluidic accessories

The connection of inlets and outlets were achieved using metal elbow capillaries that fit tightly into the punched inlets without the need for epoxy. Syringe pumps (PHD 2000, Harvard Apparatus, and Holliston, MA, USA) were used to inject liquids into the MF inlets. Connective tubing was made of perfluoroalkoxy (PFA) with outer diameter 1.6 mm (U-1148, IDEX, WA, USA), which was connected to 60mL syringes (BD Scientific, NJ, USA) via connector assembly (P-200x, P-658, IDEX, WA, USA). Liquids were vacuum degassed before injection to minimise bubble formation on-chip. Liquid delivery tubing was connected to the device inlets and outlets via metal elbow capillaries. The entire device was placed in a custom polycarbonate holder which positioned the device with the glass side up for inspection by the upright confocal imaging system. The device was placed cover slip down on an inverted microscope for imaging in transmission and fluorescence modes.

2.2. Experimental procedures

2.2.1. Microfluidic devices design and fabrication

a) Photolithography

A silicon template containing microfeatures from a thin layer photoresist (photocurable epoxy SU-8 50, Microchem Inc., MA, USA) was prepared externally based on a computer aided design prepared by our group (Figure 9). The heights of all features on the silicon mould template were 305μm, the width (w) was 2 mm and the main channel length was 32 mm, whereas the small channels had a length of 10 mm.

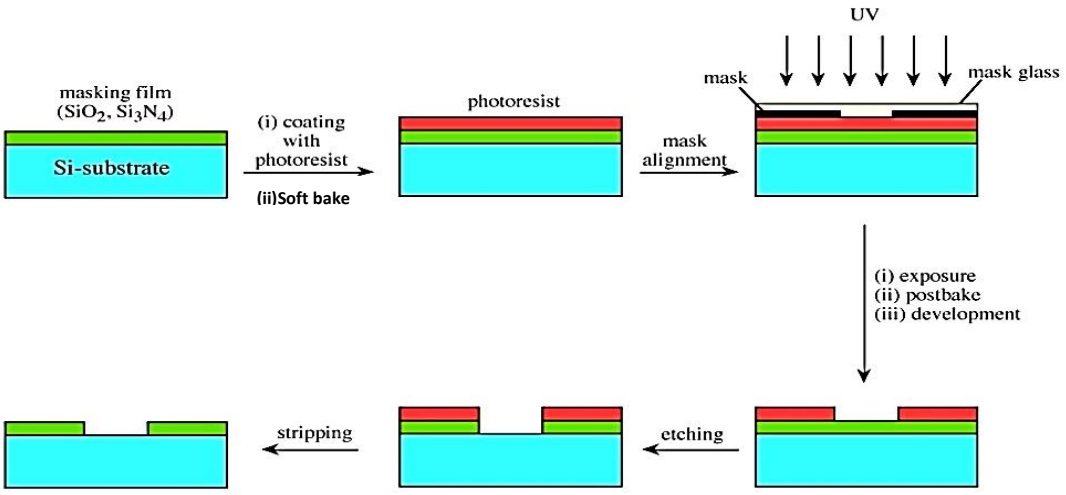

Figure 9 : Photolithography technique :(i) Deposition of photoresist on a silicon substrate. (ii) Exposure to UV light through the photomask. (iii) Post development, the UV-cured photoresist layer remains, whereas rest of the layer is washed away. (iv) Processing (etching, deposition etc.).(vi) The remaining resist is stripped[51].

b) Reactor design and fabrication

The microfluidic devices were prepared by casting uncured PDMS mixed with a cross-linker in 10:1 proportion (by weight), and poured on the silicon template and heating to 70 ^{o}C overnight. After thermal curing PDMS was demolded from the silicon template, the micro fabrication contained the features of the microfluidic channel. Each level was fabricated separately before they were aligned and bonded. (Figure10).

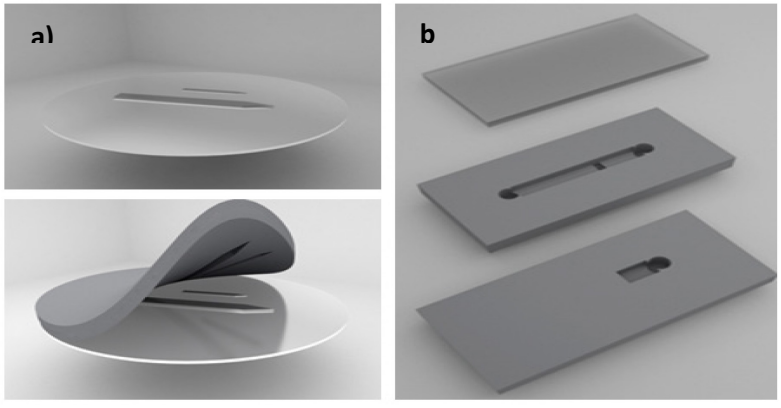

Figure 10 : Schematic for (a) a silicon master filled with PDMS and demoulded after, (b) then cutting to the desire forms used in this study and creation the holes and junction.

The MF is shown schematically in Figure 11a. Level 1 included a long measurement channel with length of L_M = 32 mm, width of w_M = 2000 μm, and a height of h_M = 305 μm. An inlet was punched at the upstream end of the measurement channel to introduce the confinement flow phase. Level 2 was aligned above Level 1 and included Inlet 2 for the introduction of the biofilm nutrient solution phase, such as bacteria-laden inoculant, growth media, or coloured liquid for visualisation experiments. The two levels were connected by a cylindrical junction hole that injected the biofilm nutrient solution phase into the measurement channel, where it encountered a flow of the confinement liquid, thereby templating biofilm growth. The biofilm templating stream width (w_T) and height (h_T) were tuned by changing the confinement flow rate and the template flow rate, Q_C and Q_T, respectively (Figure.11b, c). In this project we specify the flow rate ratio as Q_C/Q_T. The junction was fabricated by punching through the PDMS at known angle (θ) with a punch that yielded a known diameter (d=500 μm) to better specify hydrodynamic flow conditions within the measurement channel. In the results section, we used simulations to extensively explore the effect of the angle, θ, on flow template dimensions for different flow rate ratios (Figure 20). A competing effect between the $w_{T|\theta}$ and $h_{T|\theta}$ in the range $35 > \theta > 90$ was noted. However, for $\theta < 45^o$ we noted a rapid increase in w_T. Since our goal was to maximise the confinement of the template stream in the vertical and horizontal dimensions, we chose the intermediate value of $\theta = 45^o$. The measurement channel was sealed by a glass coverslip, which enabled observation of the template surface at the opposite microchannel wall using objectives that had working distances of at least 475 μm, the sum of the coverslip thickness and h_M. The device was placed cover slip down on an inverted microscope for imaging in transmission and fluorescence modes. The PDMS material is known to support gas diffusion, thereby eliminating concerns that O_2 depletion or CO_2 accumulation will impact biofilm respiration. Experiments were conducted in a temperature controlled room at 22^o +/- 2^oC.

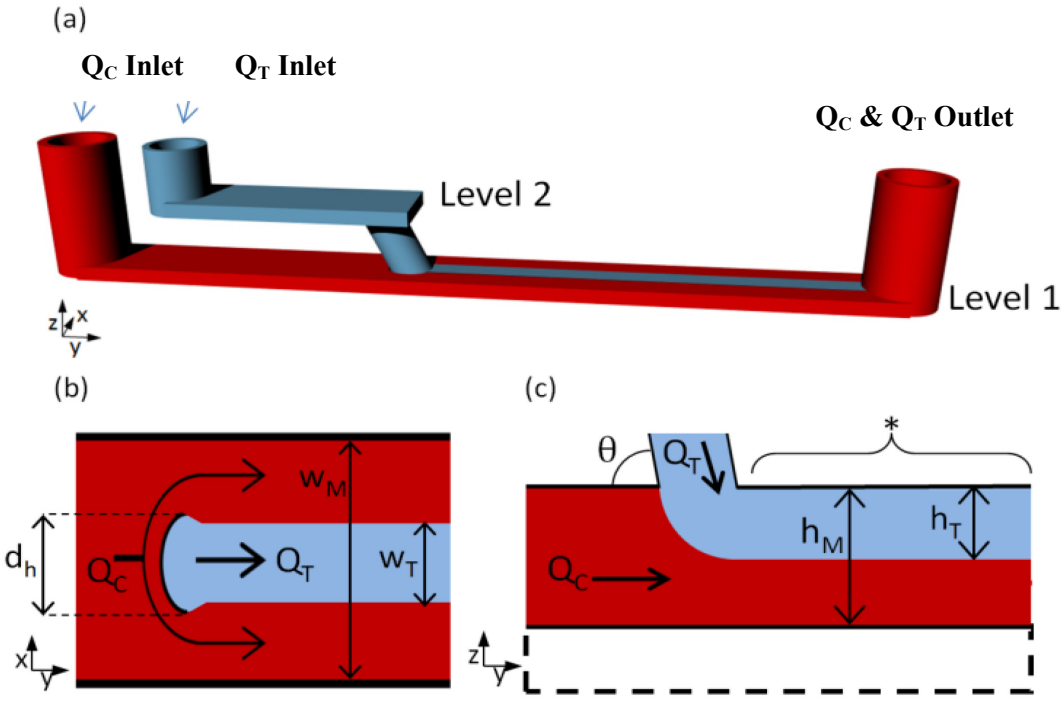

Figure 11 : **(a)** Schematic of the two-level device. The small channel in Level 2 (blue) brings the biofilm nutrient solution template stream to the measurement channel with flow rate Q_T. The inlet connected to the large (measurement) channel in Level 1 (red) brings the confinement solution with a flow rate of Q_C. Observation of the measurement channel occurs from the bottom side using an inverted microscope**. (b)** Schematic view of the cross-section in the y-x plane of the measurement channel with width w_M = 2000 µm. Junction diameter, d, was 450 µm, unless stated otherwise. Lateral confinement of biofilm template stream (blue) by the confinement stream (red) results in templated flow with width w_T. **(c)** Schematic view of the z-y cross-section of the measurement channel with height hM = 305 µm and angle θ. Vertical confinement of biofilm template stream results in templated flow with height hT. The biofilm nutrient solution template stream enters the measurement channel from the junction on the PDMS side of the channel. The bottom of the channel is sealed by a glass coverslip (dashed box) with thickness 170 µm. Biofilm cultivation occurs at the template surface (*).

2.2.2. Electroless metal deposition on microchannel walls

In order to conduct spectral imaging assay the biofilm in MFs (other project in our group), we fabricated a MF bioreactor with strong signal enhancement *via* electroless deposition of metal (silver and gold) in the bottom of the channel. Surface Enhanced Raman Spectroscopy (SERS) is a useful approach that takes advantage of plasmonic properties of metal nanostructures to in-

crease Raman scattering intensity by orders of magnitude due to strong increases in local electric fields between metal nanostructures.

A) Silver

The bottom and side walls of the of the Level 1 channel were covered with a metallic layer via electroless deposition[52]. Unlike electrodeposition, this approach enabled deposition against non-conducting PDMS microchannel surface. Electroless deposition of a silver layer was achieved by combining an aqueous solution of glucose, tartaric acid and ethanol with a Tollens reagent. Due to short shelf life, Tollens reagents were made fresh by adding ammonium hydroxide to Ag_2O precipitate prepared by mixing silver nitrate solution with sodium hydroxide solution until dissolution. The bioreactor was masked using an adhesive film (HD Clear, Henkel Corp., Düsseldorf, Germany) such that only the channel section was exposed. Before deposition, the microchannels were treated by air plasma at 600 mTorr at 29.6 W for 90 s in order to increase their hydrophilicity which allowed a better wetting by the aqueous solution. After the reaction was complete, the excess solution was removed and the channel was washed with ultrapure water and dried with filtered nitrogen. After deposition, the bottom and side walls of the channel were coated by a matt grey silver film. The mask, which protected the bonding surfaces, was then removed leaving silver in the channel only.

B) Gold

For fabrication of gold film on PDMS we used a plating solution containing 12 mM HAuCl $4H_2O$, 0.5 M $KHCO_3$, and 25 mM glucose (pH 9.3) that was injected into the square aperture PDMS mold, which jointed with a base PDMS slice, and was kept at 30^oC for 4 h to form a gold film on the base PDMS slice as shown in Figure12. Final device after electroless deposition of metal has shown in Figure 13.

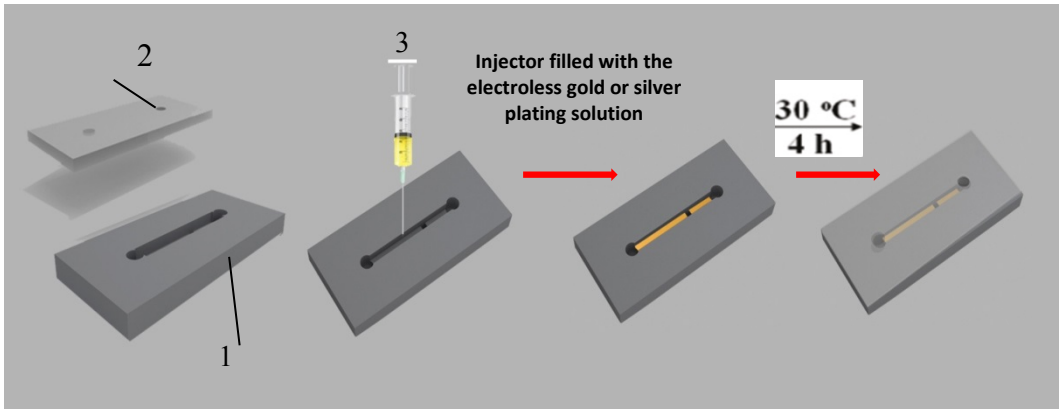

Figure 12 : Experimental procedure for electroless metal plating on PDMS. (1) PDMS framework; (2) PDMS base chip; (3) Injector filled with the electroless gold plating solution.

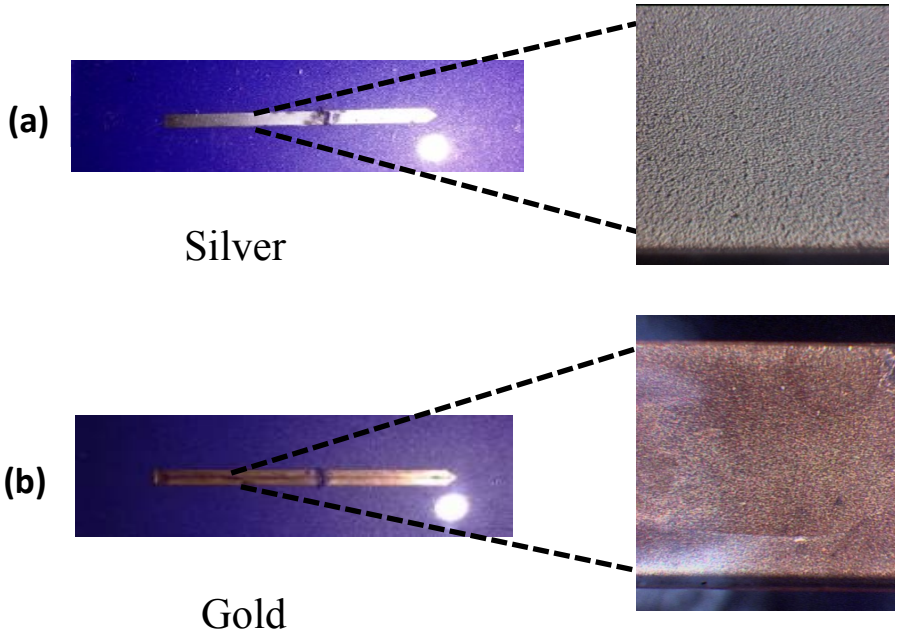

Figure 13: Microscopic images of metal deposition surface on the microchannel (a) Silver metal layer (b) gold layer deposition in the microchannel. The image was taken in dark field mode.

2.2.3. Biofilm cultivation

The pre-culture of planktonic *Pseudomonas sp*. was used as inoculum for biofilm formation. The suspended culture inoculum was obtained by shaking the cultures of planktonic *Pseudomonas sp*. in 3 mL of 5 mM growth media at 300 rpm for 18 h at 30 °C. The confinement phase consisted of the same ingredients as the growth media, but the Na-citrate concentration was 0

mM, which, therefore, did not support biofilm growth. Prior to inoculation, the MF system was disinfected with 70% ethanol for 2 h and then rinsing with sterile distilled water for 1 hour. Distilled water was displaced by flushing with sterile growth medium. Templated inoculation was conducted for 2 h. (Figure 14)

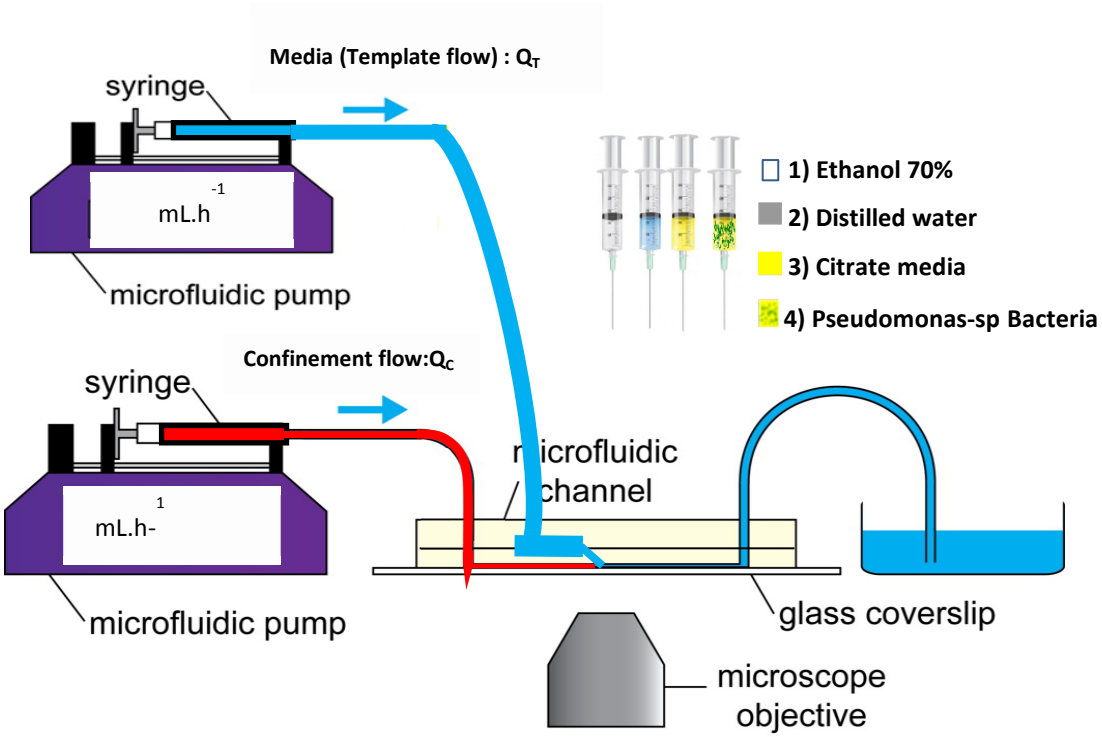

Figure 14 : A schematic of PDMS-glass microchannel and flow equipment, the channels are connected to the Teflon tubing inserted into the PDMS cast serve as the inlet and outlet connector for liquid delivery and filled with a blue dye for visualisation the template flow (QT) and red dye for visualisation of confinement flow(QC). Pumps used for micro/nanoliter flows injected. Prior to inoculation, the MF system was disinfected with 70% ethanol for 2 h and then rinsing with sterile distilled water for 1 hour. Distilled water was displaced by flushing with sterile growth medium. Templated inoculation was conducted for 2 h.

Due to the high surface area to volume ratio and due to the fact that the liquid residence time (30 s) was significantly shorter than the maximum specific planktonic growth time of *Pseudomonas sp*. CT07 GFP, it was concluded that biofilm formation was strongly favoured over bacteria growth in the planktonic state[53,54]. Following inoculation, growth media was templated

along the same path as the inoculum. Visible biofilm formations were formed after approximately 20-40 h.

Figure 15 (a) shows a transmission microscope image taken during this process. From the junction output, at the right of the image, a visible stream of planktonic-phase CT07 bacteria co-flowed downstream in a linear pattern, confined by a transparent confinement stream. Flow rates for the confinement and template flow were $Q_C = 0.3\ mL{\cdot}h^{-1}$ and $Q_T = 1.75\ mL{\cdot}h^{-1}$, respectively. This stream was fed by the small channel from Level 2. Figure 15(b) shows the same field of view under the same flow conditions taken in fluorescent mode, demonstrating that live bacteria were contained within the template phase. Here both the stream and Level 2 channel were bright due to the presence of fluorescent CT07-GFP.

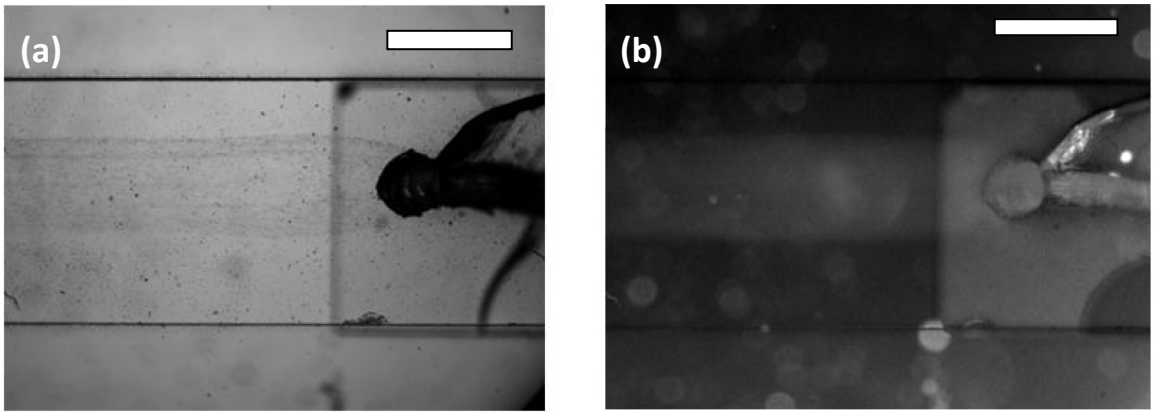

Figure 15 : Transmission image of the measurement channel in the vicinity of the junction during inoculation. Bacterial laden inoculant can be seen exiting the junction travelling downstream with flow rate $Q_C = 1.75\ mL{\cdot}h^{-1}$, $QT = 0.3\ mL{\cdot}h^{-1}$ (b) Fluorescent mode image of the same region in (a), under the same flow conditions. The CT07-GFP bacteria are visible in the template flow stream and the Level 2 channel. Scale bar is 1000 μm. Flow is from right to left in both images.

2.2.4. Image analysis of flow patterns, sessile bacteria and adhered biofilms

Optical densities and physical dimensions of template streams and the micropatterned biofilms were made using open access image analysis software (ImageJ V1.47). In all cases, background corrected images were first analysed along channel cross-sections for their pixel intensities. Often, an average cross-section profile was determined by averaging many profiles in the same vicinity. In order to avoid aberrations due to changes to ambient light levels, or low frequency oscillations in lamp brightness, background images were acquired regularly. For visualisation ex-

periments of the template solution, calibration measurements were made with the channel completely filled with the dye solution (McCormick, London, Canada) and then the transparent confinement phase. The dye concentration was determined by adding 2 drops (measured gravimetrically to be approximately 50 μL per drop) per mL of nutrient solution and the limit of detection by *in situ* transmission microscopy was determined to be equivalent to 0.1 drops per mL. Estimation of the template stream vertical path length was made using Beer-Lambert law as discussed in the results section. The maximum and minimum pixel intensities within the channel filled with only clear confinement phase liquid and dye-containing liquid, respectively, were determined in advance to be I_{max} = 2.88 x 104 (arb. units) and I_{min} = 9.9 x 10^{-3} (arb. units) using background corrected microscope images. In the case that regular background images were not attainable, for example during long-term biofilm growth experiments, normalisation was achieved using a segment of the image outside of the channel. The reduction in transmitted light as a result of biofilm development is expressed as optical density, which is defined here as the absorbance, analogous to the Beer-Lambert law. This definition of optical density has been shown previously to be proportional to biofilm mass[55].

A selected number of the COMSTAT functions and also the Bioformat macro of the ImageJ were used for the analysis of 3D reconstruction of the biofilm of the z-stack images as obtained from scanning confocal measurements in microchannel: the biovolume of each image stack ($\mu m^3\ \mu m^{-2}$), the mean thickness of the biofilm (μm) and the biofilm surface area-to-volume ratio ($\mu m^2\ \mu m^{-3}$). The biofilm surface area (um^2) (*i.e.*, the area of the biofilm exposed to the bulk-liquid) was calculated using the results of COMSTAT analysis, by multiplying the biofilm biovolume ($\mu m^2\ \mu m^{-3}$) by the xy attachment area (101,761 μm^2), and the surface area-to-biovolume ratio ($\mu m^2\ \mu m^{-3}$) for each Z-stack of images. The corresponding values obtained correlated well with the degree of biofilm development, as seen in the extent of substratum coverage and average biofilm thickness. The values were primarily utilised for qualitative purposes to identify potential relationships between the planktonic cell yield from biofilms and the different shear forces that they are subjected to, and the other hand opening a way to study growth kinetics of biofilm with different hydrodynamic conditions.

2.2.5. Colony and cell counting

Individual biofilm colonies that appeared in microscope images were counted using ImageJ analysis software. A macro was written that analysed each image in a time-series data set, which converted 16-bit grey scale images to monochromatic images that identify and count individual biofilm colonies. The macro consisted of steps for background flattening and contrast enhancement with an automatic threshold adjustment. In some cases where devices were reused and remnants of former (non-living) biofilms were present, a background subtraction was applied. An example of the original image and the contrast enhanced image showing detected colonies is shown in Figure 16a and 16b, respectively. The number of colonies was automatically registered for each image in the time-series so that the number of colonies with respect to time could be tracked. The technique is limited to the visible colonies, which in this study were relatively large due to the low power objective used (2x).

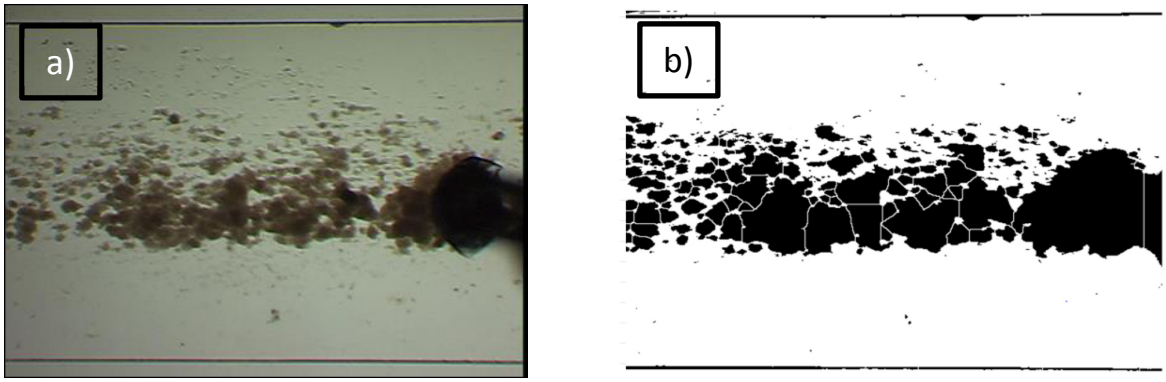

Figure 16 : (a) Greyscale microscope image of the biofilm grown under flow rates Q_C = 0.5 mL·h^{-1}, QT = 0.3 mL·h^{-1}. (b) High contrast image showing isolated colonies as detected by the image analysis macro. Flow was from right to left.

2.3.*In situ* characterisation and visualisation techniques of fluidic flow streams in addition to biofilms

Biofilms are inherently complex and heterogeneous living materials, with properties that change in space and time. In this sense, biofilms are among the most interesting and challenging materials to study analytically[56, 57]. In this section we describe the approach to characterisation.

2.3.1. Computer simulations of flow patterns

All flow simulations were conducted in three-dimensions (COMSOL Multiphysics) with a fine mesh and physics for laminar flow and transport of dilute species in an incompressible fluidic phase. Molecular diffusion of citrate molecules was simulated using diffusion co-efficient $D_{citrate} = 6.9 \times 10\text{-}10\ m^2 \cdot s^{-1}$ and we used $D_{dye} = 2.0 \times 10^{-10}\ m^2 \cdot s^{-1}$ for the diffusion of water soluble dye molecules.[39]

2.3.2. Analytical instrumentation

The dynamic nature of multiphase microfluidic systems imposes unique requirements on the time resolution of the flow characterization techniques. Table 2 summarises different experimental techniques for characterizing microscale multiphase flow as well as the spatial and temporal measurement resolutions. Intrusive measurement probes are generally not an option for micro- and nanofluidic systems. Microscopy, the most often used imaging technique, requires direct optical access to the microfluidic network. [58]

Table 2 : Experimental techniques available to study multiphase flow in microsystems with their spatial and temporal resolution.[58]

Technique	Spatial dimension	Spatial resolution	Temporal resolution/ms
Brightfield microscopy[44]	2D	~1 μm	0.2–33 ms, 18 ns (stroboscopic white light source)
Fluorescence microscopy	2D	~1 μm	33 ms, 7 ns (pulsed Nd:YAG/YLF laser)
Confocal microscopy	2D/3D (SC)[a]	~1 μm	~500 ms (2D), ~1 min (3D) ~70 ms (2D),
	2D/3D (SD)[a]	~1 μm	0.1–1 min (3D)
Transient magnetic resonance imaging (MRI)[63]	2D/3D	800 μm	150 ms
X-ray tomography microscopy (XTM)[64–66]	2D/3D	1.1–4 μm	30–90 min (3D)
	2D/3D	<100 nm	
Total internal reflectance sensor[21,67]	1D	~200 μm	0.1–1 ms
Infrared and conductivity sensor[68]	1D	Distance between probes 10 mm	0.1 ms

[a] SC = scanning confocal microscope, SD = spinning disk confocal microscope.

2.3.2.1. Optical microscopy

a) Bright-field

In this project optical micrographs of the biofilms were acquired using an inverted light microscope (Bruker, IX73, MA, USA) with bright-field illumination. Biofilms were recorded at 2x magnification (numerical aperture 0.06) whereas high resolution images of bacteria were rec-

orded at 100x magnification (numerical aperture 0.9). Images were collected using an uncooled, monochrome CCD camera (Lumenera Infinity 3-1, Ottawa, Canada).

b) Fluorescence microscopy

If at least one of the liquid phases is fluorescently labeled with an organic dye or other tracer materials, fluorescent microscopy reveals the phase distribution, the shape of the fluid interphase, or the local species concentration inside one phase in a multiphase microfluidic network. Here, imaging of green fluorescent protein (GFP) expressing bacteria was conducted on the same instrument using appropriate fluorescent excitation and filter cube.

2.3.2.2. Confocal laser scanning microscopy (CLSM)

Confocal microscopy excludes out-of-plane information in fluorescence measurements and allows three-dimensional information to be acquired section by section. The confocal technique used was laser scanning approach, where a laser beam scans the image plane line-by-line and the confocal components determine the height of the plane scanned. The intensity of the generated fluorescence is collected in a photomultiplier tube[58].

To study the effect of shear force on biofilms formation in Section 3.2.1.5, we used confocal laser scanning microscopy (CLSM). Time lapse, stack images in the Z-direction of sessile bacteria during pre-formation of biofilm were captured on an inverted Olympus Confocal microscope (FV1200) over 35 h with 1 h interval time, using a 60x Plan-Fluor oil-immersion objective, with excitation of the green fluorescent protein at 488 nm and detection of emission with a band pass 500-515 filter. All images collected were of dimension (176.13 μm × 176.13 μm) and resolution of 0.60 μm.

The extent of biofilm development in duplicate microfluidic channels in Section 3.3. was examined at 24 hour-intervals with confocal scanning laser microscopy (CLSM, Nikon Eclipse 90i, Mississauga, ON, Canada), using a 40×/0.75 Plan-Fluor objective with excitation of the green fluorescent protein at 488 nm and detection of emission with a band pass 515/30 filter. Ten microscope fields, each with an area of 101,761 μm^2 (318 μm × 318 μm), were chosen at random

along a central transect starting from the channel inlet, and a stack of images was captured in the *z*-direction at 0.60 μm intervals and stored for subsequent analysis with COMSTAT.

Chapter 3: Results and discussion

3.1. Control of flow template and generation of linear template flow patterns

3.1.1. Generating linear template flow patterns

The microchannel environment is well-suited for generating stable co-flowing streams of miscible liquids due to suppression of convective mixing[59]. Upon emerging from the junction channel, the biofilm nutrient solution template stream continued to flow downstream, confined to the centre portion of the PDMS template surface in the measurement channel by the confinement stream. However, preliminary experiments attempting to generate stable template flow patterns demonstrated poor confinement of biofilm nutrient solution due to the interaction between highly diffusive small ions leaving the template solution and other template stream molecules, such as the carbon source (citrate; Figure 17a).We solved this problem by minimising the diffusion-driven flux of small molecules out of the biofilm nutrient solution template phase by eliminating their concentration gradients at the interface between the two streams, as mention in the Section 3.1.2.1. The effect was the strong reduction of mass-transfer between confinement and template streams, resulting in a linear template solution with constant w_T (Figure 17b).

3.1.2. Optimisation of flow configuration

3.1.2.1. Reducing the effect of diffusion on template streams

In order to optimise the stability of the template pattern over long distances, we sought to minimise the diffusive mixing, which, according to Fick's law is proportional to solute diffusivity, D, and the local concentration gradient. Diffusivity of small molecules and ions such as Na^+ (D_{Na^+} = 1.3 x10^{-9} $m^2 \cdot s^{-1}$) or Cl^- (D_{Cl^-} = 2.0 x10^{-9} $m^2 \cdot s^{-1}$) used in high concentrations in growth solutions, can be significant in comparison to citrate diffusivity of 6.9x10^{-10} $m^2 \cdot s^{-1}$. Furthermore, concentration gradients between the confinement stream and the biofilm precursor template streams can be

high due to excellent flow separation in microchannels due to low Reynold's numbers. Together, these two factors could result in a large flux of molecules out of the biofilm precursor template stream into the confinement stream since the confinement stream did not contain the same highly diffusive species. Moreover, a large flux of highly diffusive molecules can result in the mass-transfer of other, less diffusive, co-dissolved molecules and suspended bacteria. This effect caused the width of the template solution (w_T) to expand as it moved down the measurement channel. Preliminary experiments using pure water as the confinement stream always resulted in large mass transfer from the biofilm precursor stream (Figure 17a). One approach to minimise variations in w_T was to increase the total flow rate without altering the flow rate ratio Q_C/Q_T. This had the effect of limiting the time for diffusion while in the measurement channel because at high velocity carried the liquid flowed through the channel too quickly before diffusion could carry many particles out of the template stream. However, this approach would prevent the utilisation of low flow velocities, which are necessary in order to probe the effect of a wide variety of flow conditions on biofilm growth rates and their properties. A second approach was to reduce the concentration gradients between confinement and template streams. This was accomplished by adding the same solutes with the same concentration to the confinement stream, which were present in the template stream, with the exception of the carbon source (citrate), which is required to support biofilm growth. As a result, diffusion was visibly reduced, which resulted in the persistence of linear template streams down the entire measurement channel even at slow flow rates (Figure 17b). We use the familiar calculation of the Péclet (Pe) number to estimate the channel distance required for complete mixing in the z and x directions for the slowest flow rate ($v = 0.36$ $mm \cdot s^{-1}$) used in this study[60]. Calculated for citrate ($D = 6.9 \times 10^{-10}$ $m^2 \cdot s^{-1}$) in the z-direction, using $Pe_z = v \cdot s\ h_M/D$ and x-direction using $Pe_x = v \cdot s\ w_M/D$, with $h_M = 0.35mm$ and $w_M = 2mm$, we determined diffusion lengths needed for complete mixing in these two directions should be 0.35 m and 1 m long, respectively. Since the measurement channel length is only 10 mm long, we conclude that the citrate molecules are strongly localized in the template stream throughout the entire length of the measurement channel.

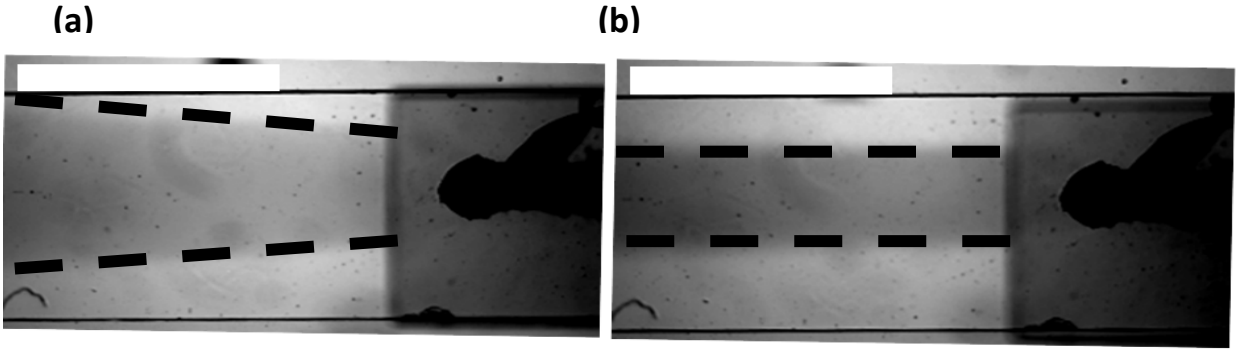

Figure 17 : (a) Transmission image of a poorly confined template solution in the measurement channel in during injection of confinement fluid consisting of pure water flowing at Q_C = 0.5 mL·h^{-1} and the dye containing template solution Q_T = 0.3 mL·h^{-1}. (b) An image of a well-confined template solution due to new confinement stream composition as discussed in the main text above. Flow conditions in (b) were the same as (a). Heavy dashed lines highlight the interface between the template and confinement streams. White boxes on the top left of the image (a) and (b) are scale bars with length 2000 μm. Flow is from right to left in both figures.

3.1.2.2. Simulation of flow patterns

We used simulations and experiments to demonstrate the versatility in generating linear template flow patterns of biofilm nutrient solution with controllable dimensions. Computer simulations verified that after a few 10's of microns downstream of the junction, the velocity and wall shear stress profiles were similar to those generated from a measurement channel with only one inlet (no junction) using a total flow rate equal to $Q_C + Q_T$. That is to say the segregated streams did not maintain memory of their initial upstream velocities. Figure 18a shows the results of a numerical simulation of the device presented here, which predicts that the shear stress (τ) along the templating wall was uniform within +/- 2% within the middle 1200 μm for the design discussed here. We used this information to determine the maximum limits on the width of the biofilm growth template solution. The co-flow patterns could also be modeled. Figure 18b shows the results of a typical simulation resulting in a template pattern, which could be used to predict details such as the shape, w_T and h_T of the template solution. As discussed in Section 3.1.2.3. we confirmed by experimentation and simulations that w_T and h_T were dependent on the flow rate ratio (Q_C/Q_T) only (Figure 19), irrespective of the overall fluid velocity. This has the

implication that the template stream dimensions can be produced using multiple Q_C and Q_T pairs, thereby opening the way for exploring the effect of applied shear force without affecting the footprint of paterned biofilm. Figures 18c and 16d show background subtracted images of the confined template flow streams passing through the microchannel at $Q_C/Q_T\big|_c = 1.67$ and $Q_C/Q_T\big|_d = 3.33$, respectively. Inspection of these images shows clearly that a decrease in template stream width was achieved from $w_{T,a} = 1064$ µm to $w_{T,b} = 700$ µm.

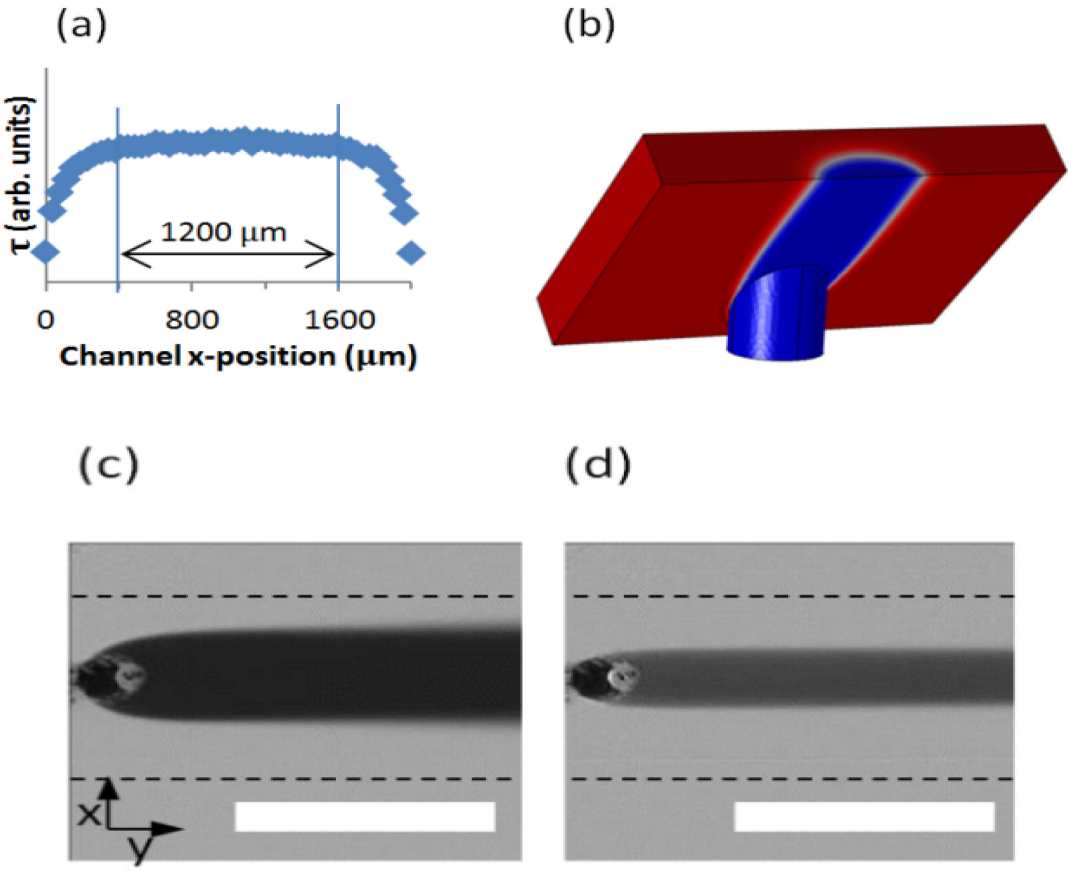

Figure 18 :(a) Shear stress (τ) profile along the templating wall for $Q_C = 2.5$ mL·h^{-1}, $Q_T = 0.6$ mL·h^{-1}. Vertical lines mark the region measuring approximately 1200 µm where τ is uniform within +/- 2%. **(b)** Results from a three-dimensional numerical simulation showing isolation of a central template flow (blue) being supplied by volumetric flow rate of $Q_T = 0.6$ mL·h^{-1} and a confinment flow (red) being supplied by a volumetric flow rate of $Q_C = 2.5$ mL·h^{-1}. The simulation is conducted in the first 1.5 mm after a junction with d = 450 µm and θ = 45°. Background subtracted images of flow streams where **(c)** $Q_C = 0.5$ mL·h^{-1}, $Q_T = 0.3$ mL·h^{-1} and **(d)** $Q_C = 1.0$ mL·h^{-1}, $Q_T = 0.3$ mL·h^{-1}. Dashed lines mark the channel walls which are invisible in background subtracted images. Scale bars in (c) and (d) are 2000 µm.

3.1.2.3. Template profiles determined by flow rate ratio, independent of total flow rate

Figure 19 shows flow profiles along the x-axis 800 µm downstream from the junction which had properties of θ = 45°, d = 450 µm. The superimposed template flow cross-section profiles show results for experiments and simulations for flow rate ratio of $Q_C/Q_T = 10$ collected at two different flow rate pairs: $Q_{C,1} = 3.0$ mL·h^{-1}, $Q_{T,1} = 0.3$ mL·h^{-1} and $Q_{C,2} = 6.0$ mL·h^{-1}, $Q_{T,2} = 0.6$ mL·h^{-1}. The two flow rates gave the same w_T and h_T despite having different total flow rates. A simulation of the heights confirms the dimensions to be expected.

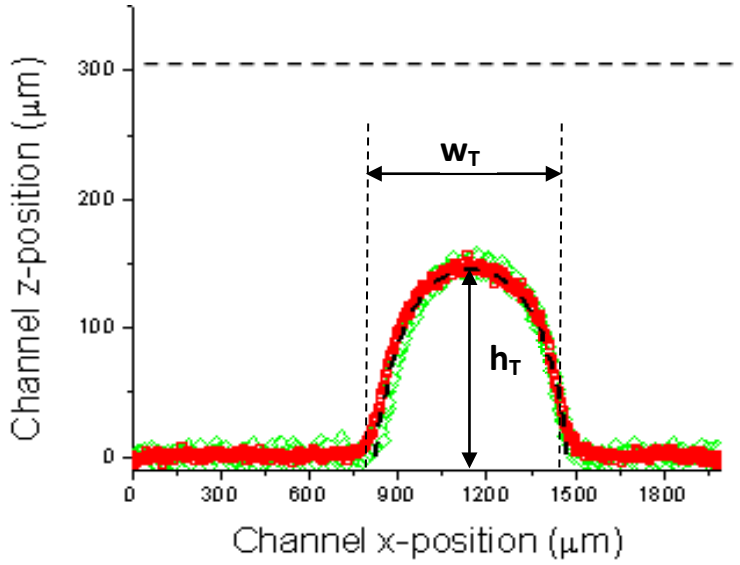

Figure 19 : Flow profile at a position 800 µm downstream of the junction for dye containing solution flowing with flow rates $Q_C = 3.0$ mL·h^{-1}, $Q_T = 0.3$ mL·h^{-1}.(red) and $Q_C = 6.0$ mL·h^{-1}, $Q_T = 0.6$ mL·h^{-1} (green). Black dashed line shows a simulation for the same flow rate ratio $Q_C/Q_T = 10$.

3.1.2.4. Microjunction fabrication parameters and their effect on the template stream

The effect that the angle between the junction hole and the measurement channel, θ, had on the template stream dimensions was determined by simulation for different flow rate ratios (Figures 20a and 20b). We noted a competing effect between the $w_T|_\theta$ and $h_T|_\theta$ in the range $35 > \theta > 90$. As θ decreased, the w_T increased gently from $w_{T|\theta=90^o}$ = 705 µm to $w_{T|\theta=45^o}$ = 725 µm for all Q_C/Q_T, but drastically increased for θ < 45 degrees. On the other hand, $h_{T|\theta}$ continuously de-

creased with decreasing θ, with a difference between $h_T|_{35o}$ and $h_T|_{90o}$ of approximately 15 µm at Q_C/Q_T = 10. In the case of both w_T and h_T, the difference in values for θ = 90° and θ = 35° was maximum at high flow rate ratios. Since our goal was to maximise the confinement of the template stream in the vertical and horisontal dimensions, we chose the median value of θ = 45°. Computer simulations predict that w_T is particularly sensitive to the diameter of the microjunction (Figure 20c). However, this factor was not extensively explored experimentally because our fabrication process was limited by the availability of a single standardised PDMS punch that resulted in cylindrical junctions with diameter, d = 450 µm.

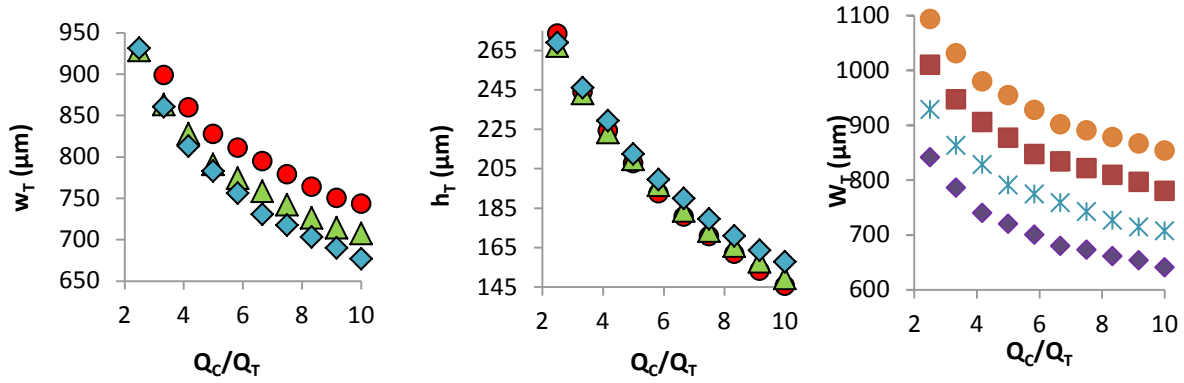

Figure 20 : (a) w_T vs. Q_C/Q_T and (b) h_T vs. Q_C/Q_T. For junction angles: 35° (red circles), 45° (green triangles), and 90° (blue diamonds). Inlet diameter was 450 µm for all simulations in (a) and (b). (c) w_T vs. Q_C/Q_T for junctions with widths: 400 µm (purple diamonds), 450 µm (blue asterisks), 500 µm (red squares), 550 µm (orange circles). All junction angles in (c) were 45°.

3.1.3. Quantitative measurement and control of flow templates

Quantitative pixel intensity profiles of the dye laden template streams were conducted at a number of flow rate ratios. Figure 21a shows results from 4 different flow rate ratios, Q_C/Q_T = (i) 10, (ii) 3.33, (iii) 0.83, and (iv) 0, where the latter is the unconfined flow of a dye laden biofilm nutrient solution only. The pixel intensity reached its highest intensity, I_{max}, in vicinity of the confinement flow streams, where pixels were bright. The pixel intensity rapidly diminished at the interface between the confinement stream and the dye containing template flow stream. The value of w_T was determined to be 703 µm, 835 µm, 1240 µm for flow rate ratios (i), (ii) and (iii), respectively. The pixel intensity reached a local minimum in the centre of the template stream.

Since diffusion-controlled mass-transfer between the template solution and the confinement solution was negligible, we concluded that the changes to the pixel intensity were due to the height of the template solution at various x-positions, h_x, not due to solution dilution. We made an estimation of h_x by applying the Beer-Lambert law to the data in the pixel intensity maps, assuming constant concentration, c,

Equation 4: Beer-Lambert equation $$\log\left({I_x}/{I_{max}}\right) = -a.c.h_x$$

where I_x is the local pixel intensity at the x-position along the channel cross-section, I_{max} is the intensity of the light passing through the channel containing only confinement-phase solution, and a is the dye solution absorptivity. With knowledge of the full channel height (305 µm), I_{min} and I_{max} we used Eq. 5 to determine $a \cdot c = 1.48 \times 10^{-3}$ (μm^{-1}). Using this approach, we converted the raw pixel, I_x, intensity into an estimated height of the template flow solution at different positions along the channel cross-section. The maximum height at the centre of the template stream was taken as h_T. Three cross-section profiles are plotted in Figure 21b. For high values of Q_C/Q_T, we noticed that the peaks in h_x became "flattened" due to the resistance of the confinement fluid to deformation as it was compressed against the glass coverslip by the template solution. These plots allowed us to experimentally estimate w_T and h_T for different flow rate ratios. Figure 21c shows the variations in w_T and h_T with Q_C/Q_T and their comparison to simulation.

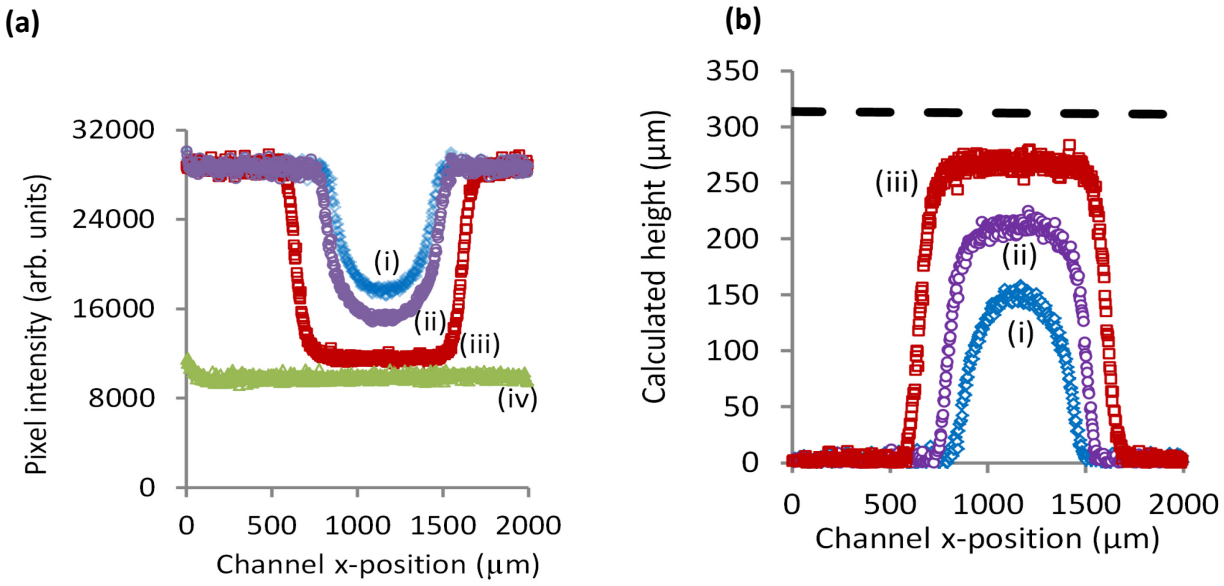

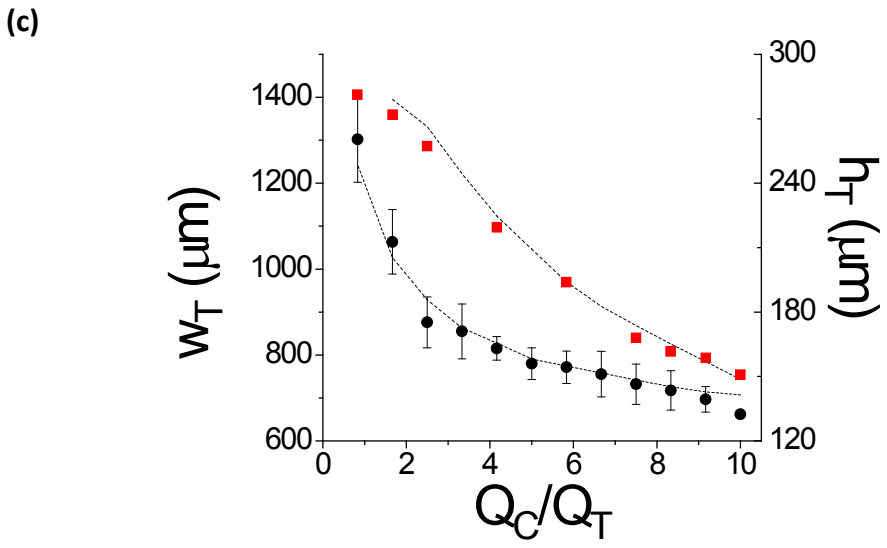

Figure 21 :(a) The results of measurements of the raw pixel intensity along the channel x-direction of dye laden template stream, (flow rate Q_T) being confined by a clear confinement stream (Flow rate Q_C) with flow rate ratios (Q_C/Q_T) of (i) 10, (ii) 3.33, (iii) 0.83, (iv) 0. Results for confinement liquid only (Q_C/Q_T = infinity) are not shown because they had the same values as I_{max}. **(b)** Plot of h_T at different Q_C/Q_T values as calculated using Eq. 4 for 3 flow rate ratios (i), (ii) and (iii), in (a). The dashed line is the maximum channel height as calculated from Eq. 4 using using I_{min} shown in (a). Flow rate ratios in (a) and (b) were generated using constant Q_C = 0.6 mL h^{-1} and adjusting Q_T accordingly. **(c)** Changes to w_T (black circles) and h_T (red squares) with Q_C/Q_T for FT-μBRs with θ = 45° and d = 450 μm. Error bars for w_T and h_T were generated by averaging the results from 3 separate experiments. Error bars for h_T are smaller than the data points. Results from simulations (dotted lines) using same conditions as the experiment, but difffusion is turned off to reduce computation time. Calculated heights using Beer-Lambert law. Maximum channel height (dashed line) was determined using (iv) in (a).

3.2. Control over BF growth dimensions and quantification biofilm growth using advanced optical image analysis

3.2.1. Templated growth of BFs

We cultivated biofilms in the FT-μBR at various values of Q_C/Q_T to demonstrate the ability to control the widths of patterned biofilm. Figures 22a,b show images of two biofilms acquired 50 h after inoculation, which were cultivated under the flow rate ratios $Q_C/Q_T|_a$ = 3.33 and $Q_C/Q_T|_b$ = 1.67.

We analysed their optical densities between 800 μm < y < 2300 μm after the junction to obtain an averaged cross-section profile of the biofilm (Figure 22c), which enabled accurate measurements of the biofilm width. Using this approach, the widths of the biofilms in Figures 22a and

22b were measured to be 850 µm and 1063 µm, respectively. These values compared well with the measurements and simulations of the biofilm nutrient solution template width, w_T. (Fig22)

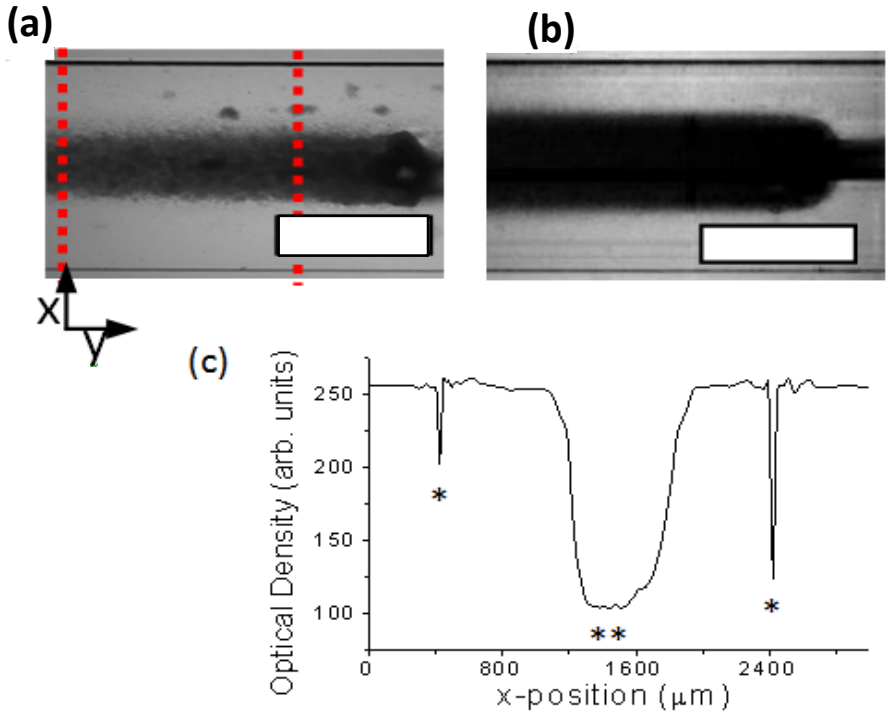

Figure 22 : Optical images of templated biofilms at t = 50 h after inoculation for flow rates: (a) $Q_C|_a$ = 1.0 mL·h^{-1}, $Q_T|_a$ = 0.3 mL·h^{-1}, (b) $Q_C|_b$ = 0.5 mL·h^{-1}, $Q_T|_b$ = 0.3 mL·h$_{-1}$. Average biofilm widths were: (a) 850 µm, (b) 1063 µm. Red dashed lines show the region between 800 µm < y < 2300 µm. Flow in (a) and (b) was from right to left and scale bars are 1000 µm. (c) Average pixel intensity profile along the x-direction of the channel of the biofilm (**) shown in (a). Peaks marked with * show the channel walls. Base line correction was done to account for slight differential illumination across the channel. The curve was the average of multiple individual cross-sections generated between 800 µm < y < 2300 µm.

Figure 23a shows an image of the entire measurement channel, which was stitched together from 4 separate images before background normalisation. The image of the biofilm was acquired 43 hours after inoculation under flow conditions Q_C = 0.25 mL·h^{-1}, Q_T = 0.3 mL·h^{-1}. Due to laminar flow and the resulting the low mass transfer of citrate molecules between the confinement and nutrient template streams, the template stream maintains good long-range patterning throughout the entire measurement channel, despite the low flow rate. We also note the progressive reduction in the optical density of the biofilm along the length of the measurement channel due to up-

stream nutrient depletion (Figure 23b). Given the channel cross-section area 0.61 mm^2, the total flow velocity was calculated to be v = 0.36 $mm \cdot s^{-1}$ and the maximum liquid residence time in the 12 mm templating region of the channel was approximately 30 s. The resulting biofilm optical density, and therefore its mass density, decreased exponentially during the first 3 mm downstream of the junction, and then nearly linearly until the end of the channel. This suggests different mechanisms for citrate mass-transfer, for example rapid consumption near the biofilm/bulk liquid interface, leading to a depletion zone, and subsequent diffusion limited influx of citrate molecules into the depletion zone from the bulk liquid template stream. The FT-µBR will be used in future studies to accurately investigate these questions and the role of the hydrodynamic environment on kinetics of citrate consumption.

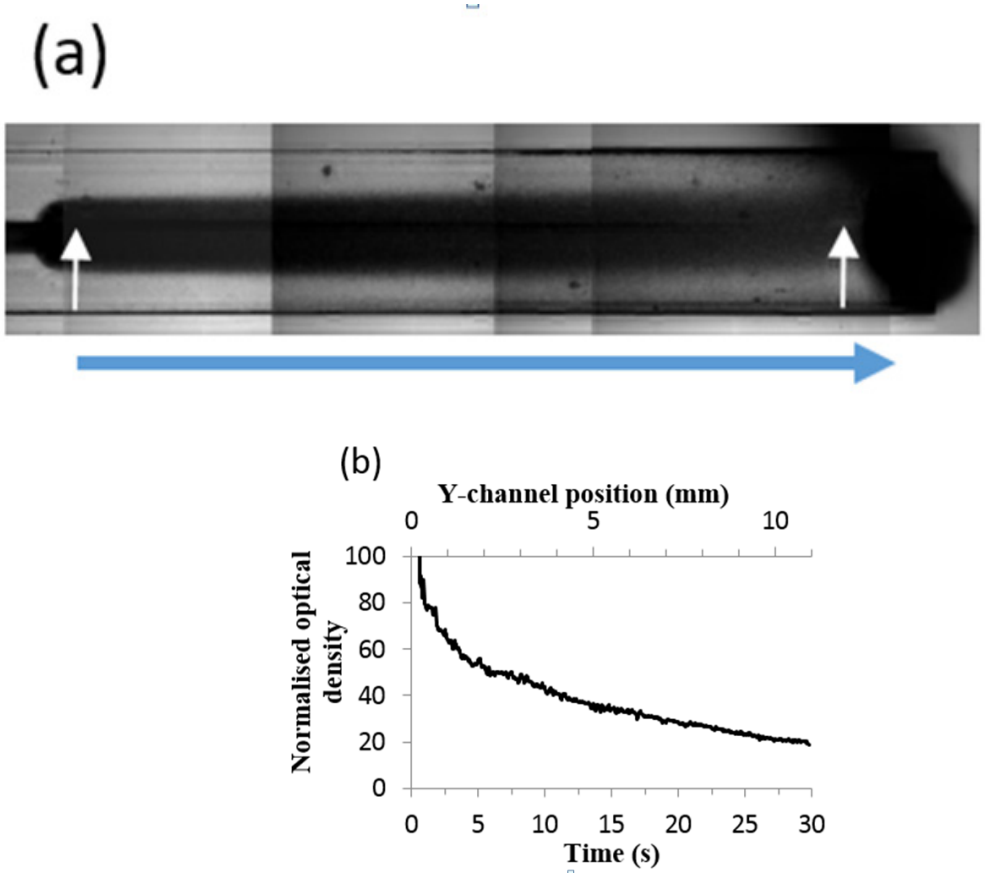

Figure 23 : **(a)** Stitched image showing the complete measurement channel containing a biofilm 43 h after inoculation. Hydrodynamic growth conditions were Q_C = 0.25 $mL \cdot h^{-1}$, Q_T = 0.3 $mL \cdot h^{-1}$. White arrows mark the y_{min} and y_{max} for optical density measurements in (b). Blue arrow indicates the direction of flow was left to right. **(b)** Normalised optical density measurements based on x-averaged pixel intensity at different positions in the channel. The contact time between the nutrient solution and the biofilm is noted on the lower axis.

3.2.1. Time dependant growth studies

Figure 24a shows time-series micrographs (i)-(vii) of flow-templated biofilms grown under flow conditions $Q_C = 1.0\ mL \cdot h^{-1}$, $Q_T = 0.3\ mL \cdot h^{-1}$ over the time interval $0\ h < t < 60\ h$. The process starts with the flow template inoculation of live bacteria, followed by culture under template flow of a biofilm nutrient solution (Figure 24a(i)). The biofilm growth initially consists of small disparate colonies within the flow template region (ii). Soon, these colonies begin a rapid expansion phase marked by colony growth and merging to form a continuous biofilm (iii)-(v). The images in this time interval reveal that there is a wide variance in the pixel intensity. Finally, the continuous biofilm becomes more uniform and opaque during a mature growth phase (vi)-(vii). Figure 24b shows quantitative measurements of the mean pixel intensity for a biofilm grown under flow conditions $Q_C = 0.5\ mL \cdot h^{-1}$ $Q_T = 0.3\ mL \cdot h^{-1}$. The standard deviation in their intensities was also calculated. We defined three key times in each pixel intensity curve: a slow growth phase during which micro colony formation is initiated, but does not strongly impact pixel intensity values, similar to the lag phase in batch cultures (*); a rapid growth phase with consequent increases in cell numbers and extracellular polymeric materials resulted in increased light scattering and rapid changes to pixel intensity (**); and a mature phase where biofilm cell growth, and potentially EPS (extracellular polymeric substances), is balanced by release from the biofilm (***), resulting in near-constant pixel intensity. The results of a colony counting image analysis algorithm that was run on the same data set, demonstrated the relationship between the merging of biofilm colonies and the onset of the mature phase (Section 3.2.1.3,). We noted maximal values in the standard deviation of the pixel intensity near the curve inflection point, the point where the change in pixel intensity vs. time was greatest, likely because, asynchronous growth of differently sized biofilm colonies prior to colony merging into a confluent biofilm. The minimum standard deviation in the pixel intensity was observed when the biofilm had reached the mature phase. We note that the characterisation method employed here limits our ability to monitor the biofilm development after regions become opaque. Not all biofilms became

opaque, and this effect could be mitigated, to a large degree, by changing exposure time or illumination intensity.

The FT-μBR enabled comparative studies of biofilm growth under different flow conditions. Figure 24c shows changes to the normalised optical density for three different flow rates (i) 0.8 $mL \cdot h^{-1}$, (ii) 1.3 $mL \cdot h^{-1}$, (iii) 1.6 $mL \cdot h^{-1}$, which produced an applied shear stress against the growing biofilms of 17.4 mPa, 25.2 mPa, 29.8 mPa, respectively. The effect of increasing shear stress is noted in terms of two effects. The first effect observed with increasing wall shear stress is the difference in biofilm rate of growth during the rapid (exponential) growth phase. We estimated the rate of growth by measuring the slope of the optical density curves during the rapid growth phase, which is nearly linear. The results showed that biofilm rate of growth in this phase also increased linearly with the applied wall shear stress (Section 3.2.1.1, Figure 25). This is consistent with the fact that nutrient penetration into the biofilm *via* advection is influenced by hydrodynamic environment.[61] The second observable effect of increasing shear is that the time duration of the lag phase (t_{lp}) is longer. Lag phase is the time before measurable biofilm development occurred (similar to the lag phase in batch culture). As described elsewhere, this time was defined as the time between the end of inoculation (t = 0 s) and when the tangent line of the maximum slope of the optical density curve intersected with the x-axis[62]. We noted that t_{lp} varied linearly with the applied shear stress in the range of approximately 17 mPa to 30 mPa, with a slope of 1.9 $h \cdot mPa^{-1}$ (Section 3.2.1.2 Fig.26). A possible explanation for this observation is the reduced probability of cells to overcome the higher shear in order to successfully attach to the surface, which in turn leads to a longer time to reach the critical cell mass and EPS scaffolding needed for surface modification and biofilm proliferation.

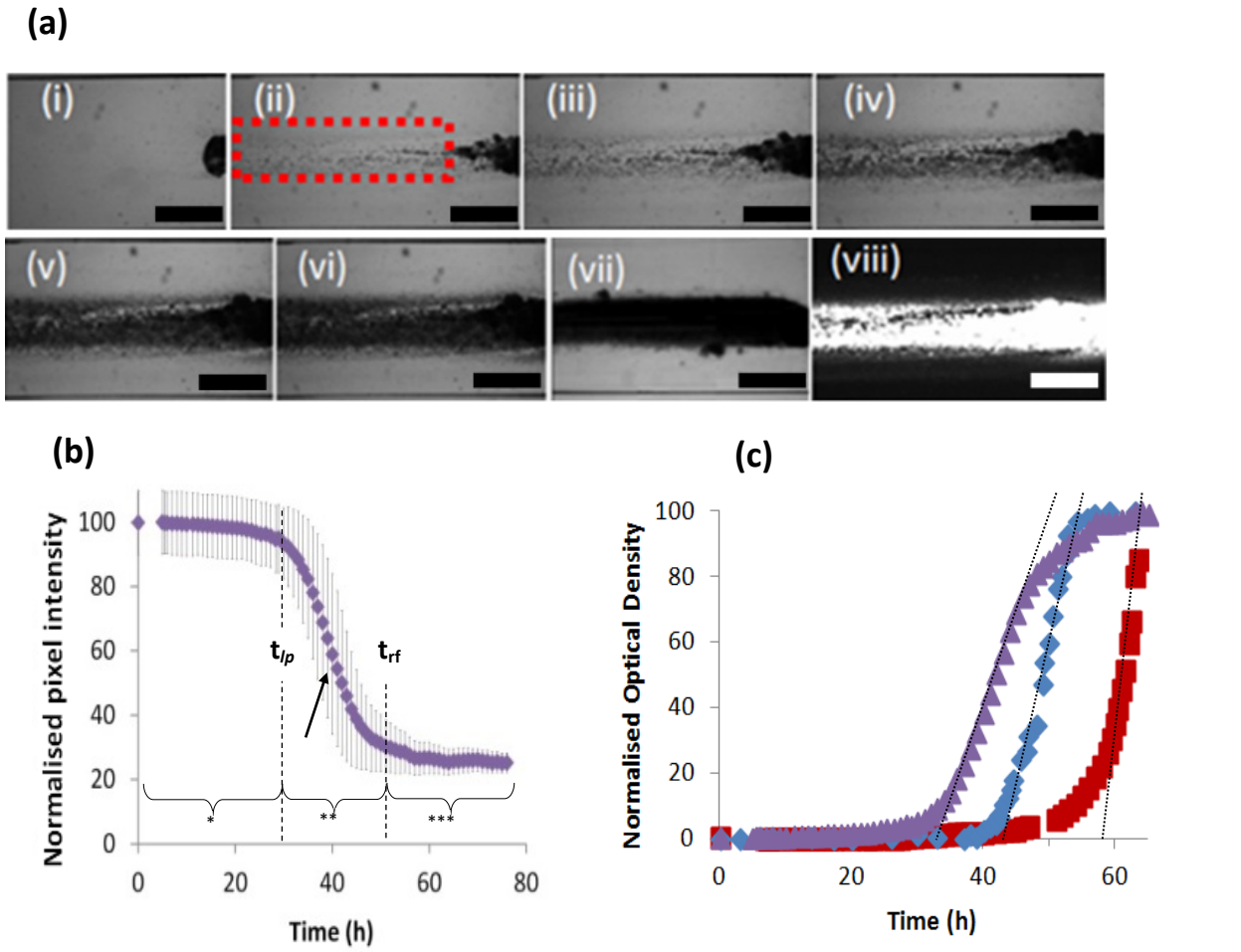

Figure 24 : (a) Images of the growing biofilm in the measurement channel at the times (i) 0 h, (ii) 37.0 h, (iii) 44.5 h, (iv) t = 48.1 h, (v) t = 49.8 h, (vi) t = 51.0 h and (vii) t = 59. 1h following inoculation. Flow conditions were Q_C = 1.0 mL·h^{-1}, Q_T = 0.3 mL·h^{-1}. The image (viii) is the fluorescent mode image of (vi), included here to demonstrate the potential to use fluorescent markers in future studies. Scale bars are 1000 µm. The red box in (ii) shows the area in which optical analysis took place for all images. Flow is from right to left. **(b)** Mean pixel intensities obtained within the red box in (a), showing the lag / adaptation phase (*), rapid growth (**) and mature phase with little or no net biofilm accumulation (***). Flow conditions were Q_C = 1.0 mL·h^{-1}, Q_T = 0.3 mL·h^{-1}, flowing from right to left. The rapid growth phase starts at t = t_{ri} and ends at time t = t_{rf}. The arrow points to an inflection in the curve where the rate of change of mean pixel intensity is the highest and the standard deviation is the greatest. Error bars give the standard deviation in the pixel intensities. **(c)** Time varying optical density measurements of biofilms grown under total flow rates 0.8 mL·h^{-1}(purple tringles), 1.3 mL·h^{-1} (blue diamonds), and 1.6 mL·h^{-1}(red squares). Linear portions of the growth curves measured during the rapid growth phase highlighted with dotted lines. Error bars in (c) are excluded for clarity.

3.2.1.1. Growth rate with varied applied shear stress

As discussed in the previous section, the slope of the rate of increase of optical density plot with time is nearly linear during the growth phase. Figure 25 shows relationship between slope of the

growth curves and the applied shear stresses. As optical density and biomass density are proportional, but the proportionality constant is unknown, the y-axis values are arbitrary.

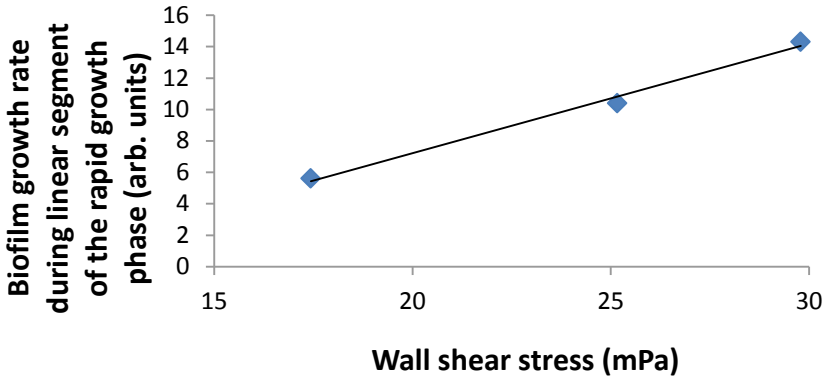

Figure 25 : Relation between change in the optical density (proportional to biofilm growth rate) and the applied wall shear stress. A linear trend line is fit to the data points.

3.2.1.2. Lag time of Biofilm formation under varied shear stress

We noted a lag phase between inoculation and the observation of measurable biofilm development (*via* increases to optical density in bright field microscope images). We observed a linear relationship between the time duration of the lag phase (t_{lp}) and the wall shear stresses in the range of 17 to 30 mPa, which were applied to the FT-µBR during cultivation (Figure 26). We attribute this to the increasing time required for surface modification by the bacteria in order to enhance wall adhesion in shear flow environments.

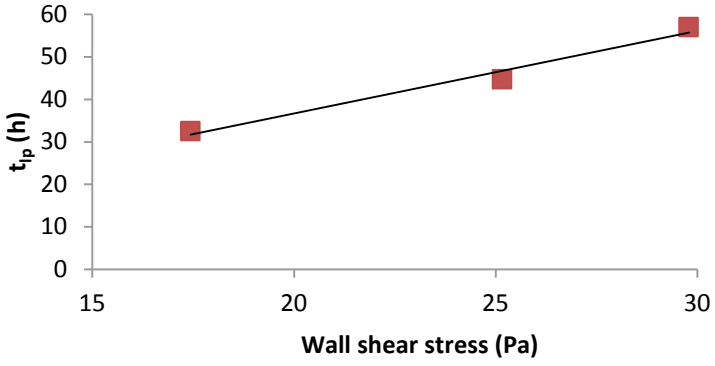

Figure 26 : Relation between the length in time of the lag phase and the wall shear stress. Slope was found by fitting linear trend line which had slope of 1.9 h·mPa^{-1}.

3.2.1.3. Relation between the number of biofilm colonies and biomass density

Comparing the changes to biomass density with the number of colonies can be informative from the perspective of understanding the mechanisms at play during initial stages of biofilm growth. Figure 27 shows the pixel intensity from in data shown in Figure 24b with the colony count superimposed on the same time scale. As can be seen, the number of individually resolved colonies is a maximum near 45 h after inoculation. This is the approximate time for the transition from rapid growth to mature growth phase.

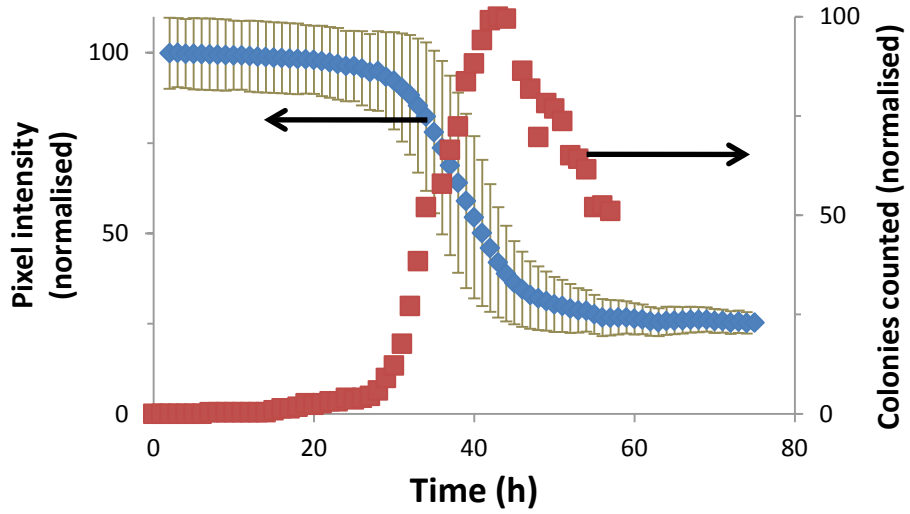

Figure 27 : Pixel intensity data set from Fig. 24b (blue diamonds) with results of colony counting superimposed on the same time scale (red squares)

3.2.1.4. Cell counting of early stage biofilm development by high resolution microscopy

As noted above, the lag phase between inoculation and the biofilm growth is likely due to the time required for surface conditioning by the bacteria to achieve good adhesion in the increasing shear flow environment. To monitor bacterial growth in advance of observable changes to low resolution optical density experiments, we used a high numerical aperture (0.9), high magnification (100x) objective. We monitored the growth of the pre-biofilm sessile bacteria against the FT-µBR glass coverslip in an unconfined template stream of media solution containing citrate concentration of 10 mM. Figure 28 is comprised of micrographs of bacteria at the adhesion surface at

different times after inoculation, for the flow rate Q_{Tot} = 0.17 mL·h^{-1}. We used software-based cell counting macros to determine the number of bacteria in the field of view with time until it became difficult to resolve individual bacteria, due to significant growth out of the focal plane. Using this counting method, we obtained the curves in Figures 29. As seen in the micrographs in Figure 28, cell density remained low for an initial period and then increased rapidly until biofilms could be seen via changes to optical density. We note that the initial time during which the bacteria count remained relatively low, was longer for Q_{Tot} = 0.8 mL·h^{-1} compared to Q_{Tot} = 0.17 mL·h^{-1}. Future detailed studies of growth kinetics using the FT-μBR will monitor the pre-biofilm sessile bacteria population sizes in time within the template region for different conditions, such as flow rates, concentrations, surface materials and temperatures.

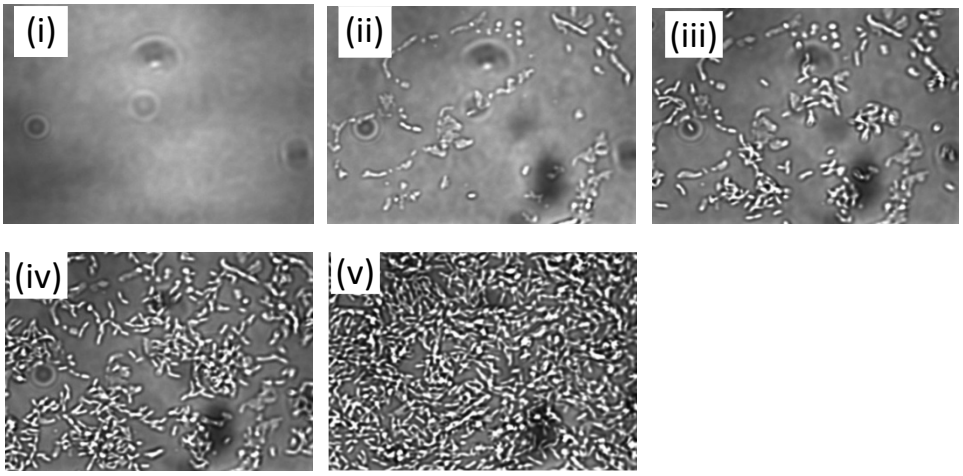

Figure 28 : High resolution bright field images of the sessile bacteria immediately following inoculation at times $t_i < 0$ h (pre-inoculation), $t_{ii} = 0$ h, $t_{iii} = 21$ h and $t_{iv} = 30$ h, $t_v = 40$ h for $Q_T = 0.8$mL·h^{-1}. The Figure (v) is representative of an overcrowded field of view, for which bacterial counting was not possible. Images were acquired using 100x objective. Scale bar is 2 μm and the field of view in all images is 65 μm^2.

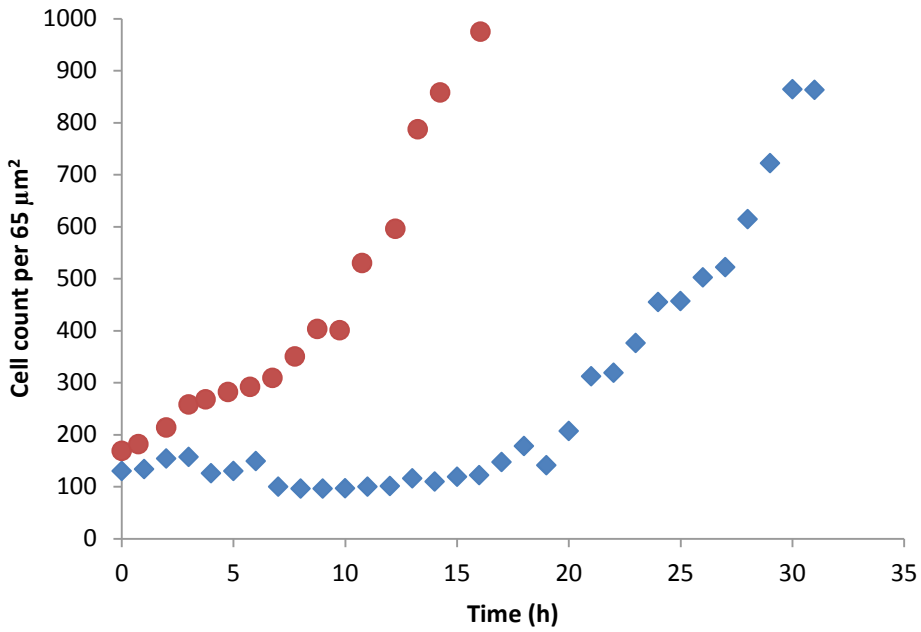

Figure 29 : Cell counting during the pre-biofilm phase for Q_{Tot} = 0.17 mL·h^{-1} (red circles) and Q_{Tot} = 0.8 mL·h^{-1} (blue diamonds). Data were automatically acquired each every hour and cell counting was accomplished using automated detection and counting macros.

3.2.1.5. Cell counting of early stage biofilm development by high resolution CLSM

In order to complete the tests mentioned in the previous section and have more precise information, three-dimensional biofilm growth, inside of the channel detected with the same conditions as test before (3.2.1.4) with the flow rate 0.8 mL·h^{-1}**.**

Time lapse, Z-stack images of sessile bacteria were captured over 35 h after inoculation of bacteria in the microchannel with 1 h interval time (Figure 30), on an inverted Olympus Confocal microscope using a 60x Plan-Fluor oil-immersion objective . All images collected were of dimension (176.13 µm × 176.13 µm) and resolution of 0.60 µm..The results of the cell counting are shown in Figure 31.

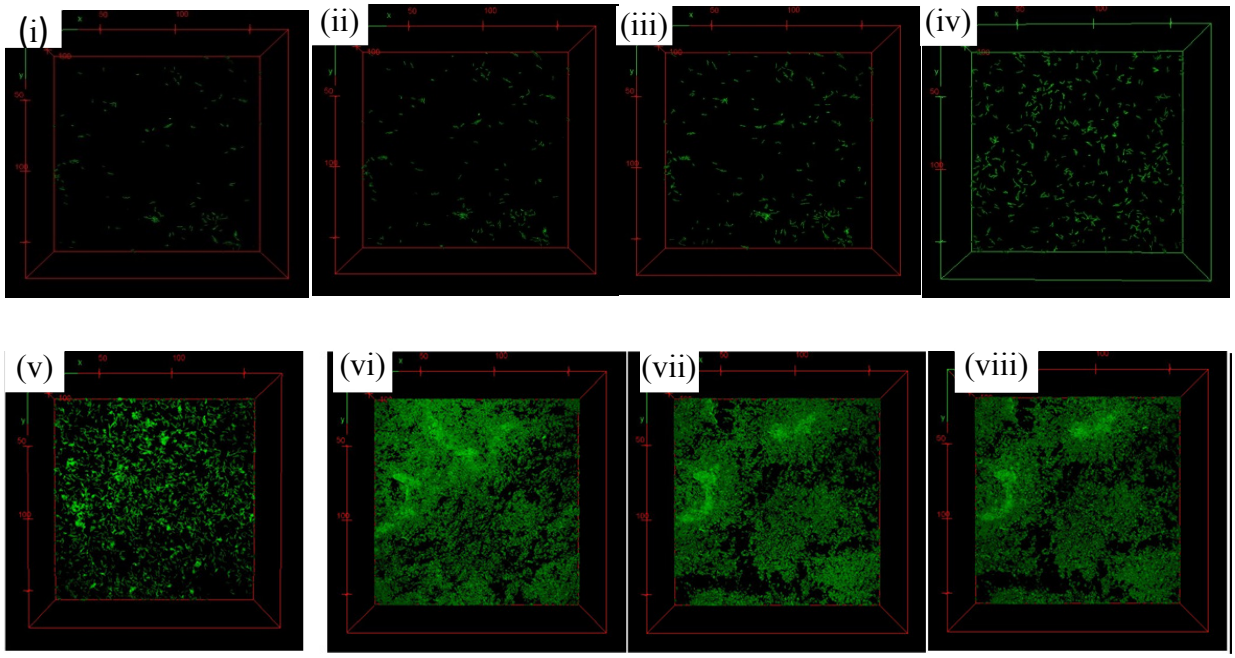

Figure 30 : High resolution (what zoom on objective) CLSM images of the sessile bacteria immediately following inoculation at times $t_i < 0$ h (pre-inoculation), $t_{ii} = 1$ h, $t_{iii} = 6$ h and $t_{iv} = 8$ h, $t_v = 25$ h t_{vi}=32, t_{vii}=34, t_{viii}=35 for $Q_T = 0.8 mL \cdot h^{-1}$. Need a scale bar.

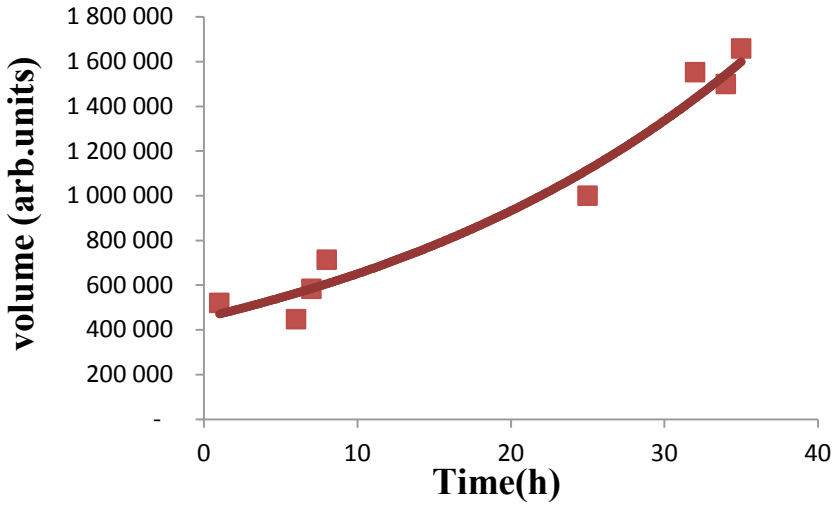

Figure 31: Cell counting during the pre-biofilm phase for $Q_{Tot} = 0.8 mL \cdot h^{-1}$. Data was automatically acquired over 35 h and cell counting was accomplished using automated detection and counting macros. The red line is exponential trend line for eye guidance.

3.3. Microfluidic studies of shear induced cell proliferation from biofilms

3.3.1. Biofilm-Associated Planktonic Cell Production

Biofilm development and the associated planktonic cell yield were determined at four different growth medium flow velocities (28.6×10^{-3}, 29.1×10^{-2}, 48.5×10^{-2}, 97.0×10^{-2} mL h^{-1}) resulting in laminar flow in the channels. The corresponding average shear stresses were calculated by equation of shear stress indicated in part 1.3.3.2, and are noted in Table 3 together with Reynolds number for each of the four flow rates.

Table 3 : The various laminar flow velocities applied to biofilms developing in the microfluidic channels with corresponding average shear rates and Reynolds number.

Regime	1	2	3	4
Flow velocity (ml.hr^{-1})	**0.0286**	**0.291**	**0.485**	**0.970**
Average shear stress (mPa)	**9.42**	**95.9**	**160**	**320**
Reynolds number	**0.0368**	**0.375**	**0.624**	**1.25**

The bulk-liquid flow rates at which the growth medium was supplied to the microfluidic channels resulted in dilution rates that greatly exceeded the maximum rate at which *Pseudomonas* sp. strain CT07*gfp* can replicate when growing in suspension. Consequently, it is assumed that an independently replicating planktonic population of bacteria would be incapable of persisting in the bulk-liquid phase of the channels. The culturable cell numbers enumerated from the effluent samples were thus presumed to originate from surface-associated growth. The majority of the detached biomass particles in the effluent consisted of single or dividing cells, whereas the presence of large sloughed aggregates of cells were rarely observed (data not shown).

Comparatively small differences in the rate of planktonic cell production by biofilms subjected to a large range of shear stresses is evident from Figure32, apart from the lowest shear rate (9.42 mPa) where the numbers of cells present in the effluent were consistently lower. Statistical analysis indicated a significant difference between the cell yield from biofilms subjected to the lowest

shear stress (9.42 mPa) and those at higher shear stresses ($P_{0.05} = 1.36 \times 10^{-5}$). The reduced flux of nutrients to the biofilm was probably a major cause for the lower cell yield, which is in agreement with the earlier observations regarding the link between carbon utilization and biofilm detachment[63]. The rate of planktonic cell production generally increased slightly over the course of incubation and peaked at the production of ~10^7 cells per cm^2 of internal channel surface area per hour, for biofilms subjected to the higher shear rates (95.9 mPa, 160 mPa and 320 mPa). Two-factor ANOVA and subsequent Post Hoc analysis indicated a statistically significant higher yield from 96 hour-old biofilms subjected to 320 mPa than younger biofilms exposed to the same shear stress ($P_{0.05} = 1.14 \times 10^{-5}$). This observation is somewhat unexpected, since the cell yield generally exhibits only minor fluctuation once biofilm development reaches a steady state after 3 to 4 days of cultivation.

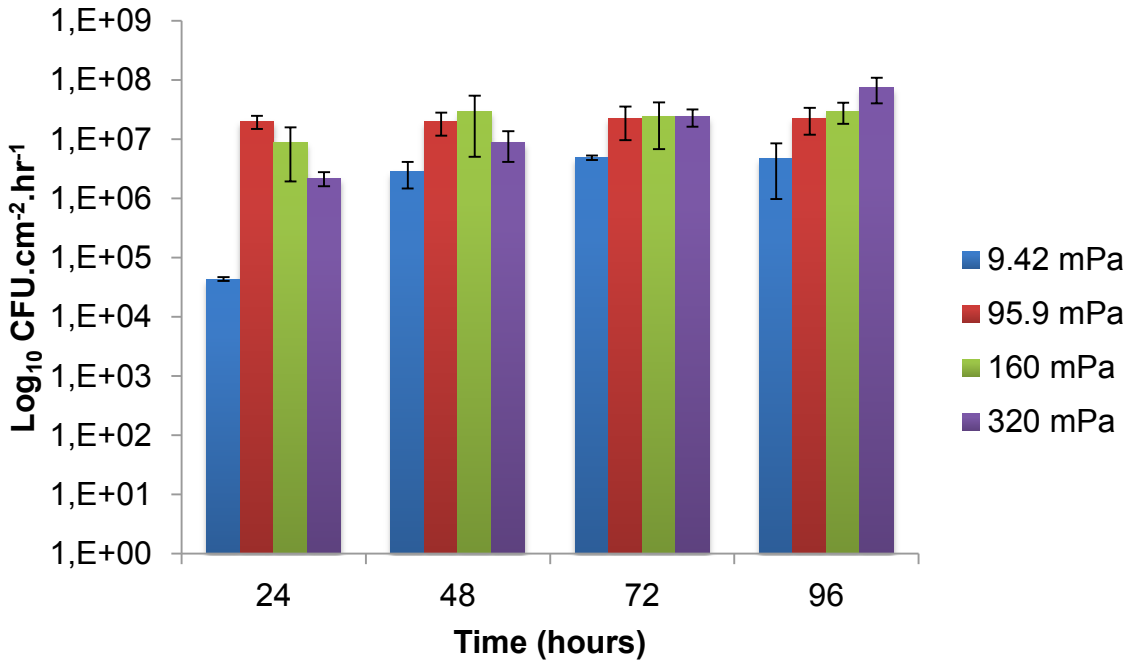

Figure 32 : The viable cell numbers (colony forming units (CFU) per mL of effluent) released from biofilms, normalized with respect to the bulk-liquid flow rate (mL h^{-1}) and total substratum area (cm^2) available for cell attachment and biofilm development. Biofilms were allowed to develop in replicate microfluidic channels for up to 96 h under different bulk-liquid flow velocities; thereby subjecting the biofilms to a wide range of average fluid shear rates (mPa). Error bars indicate the standard deviation of samples taken from replicate biofilms (two experimental rounds, with each round consisting of biofilms growing in two microfluidic channels).

3.3.2. Biofilm Morphology

The extent of biofilm development was quantified by CLSM and subsequent analysis of average biofilm thickness with COMSTAT (Figure 33). Biofilm development under the lowest average shear rate (9.42 mPa) was significantly lower, with a decline in the amount of attached biomass over the course of 96 h (Figure 34), likely due to a lack of nutrients and/or oxygen. In contrast, the average thickness of the biofilms exposed to higher shear rates (and thus higher substrate loading rates) generally increased due to attached cell growth.

Higher flow velocities increase substrate supply and thus availability, which supports the accumulation of greater amounts of attached biomass. However, higher flow velocities also exert more significant shear stresses on the biomass, leading to a greater probability of biomass detachment. The highest shear rates applied in this study were not sufficient to prevent biofilms from developing at the glass surface, although a decrease in the average biofilm thickness at 96 h (Figure 33) may suggest that the narrowing of the channel's cross section due to biofilm development on the channel walls increased the bulk average shear rate to such an extent that a portion of the attached biomass was unable to resist shear mediated detachment. Despite the reduction in average biofilm thickness, the yield of planktonic cells to the bulk-liquid was observed to increase, (Figure32), which suggests that biofilms maintain their proliferation function under a wide range of flow conditions and biofilm form. Higher flow velocities increase substrate supply and thus availability, which supports the accumulation of greater amounts of attached biomass. However, higher flow velocities also exert more significant shear stresses on the biomass, leading to a greater probability of biomass detachment. The highest shear rates applied in this study were not sufficient to prevent biofilms from developing at the glass surface, although a decrease in the average biofilm thickness at 96 h (Figure 33) may suggest that the narrowing of the channel's cross section due to biofilm development on the channel walls increased the bulk average shear rate to such an extent that a portion of the attached biomass was unable to resist shear mediated detachment. Despite the reduction in average biofilm thickness, the yield of planktonic cells to the bulk-liquid was observed to increase, (Figure 32), which suggests that biofilms maintain their proliferation function under a wide range of flow conditions and biofilm form.

The development of chains of cells and the formation of large ridges of matrix-embedded cells interconnecting individual microcolonies were also observed. As could be expected, these ridges

or filaments were oriented parallel to the direction of flow, as could be noted for 72 and 96 hour-old biofilms subjected to a shear stress of 95.9 mPa and 96 hour-old biofilms subjected to 160 mPa (Figure 34).

CLSM projections (Figure 34) illustrate the morphology of biofilms developing under the different shear stresses. The use of the 40× objective during microscopy facilitated the capture of the variation in biofilm morphology along the majority of the entire cross section of each channel. The reduction in local shear rates in the vicinity of the corners of the channels (where the glass substratum meets the walls of the microfluidic channels), compared to the higher shear removal forces operating along the center of the channel, allowed more biofilm biomass to accumulate near the wall. This is evident from the large amounts of green fluorescent biomass present towards the right hand of some of the projections (95.9 mPa at 72 and 96 h,Figure 34). The heterogeneity in the amount of biomass developing along the cross section (perpendicular to flow), as well as the length of each channel (in line with the flow from in- to outlet), is reflected in the large standard deviations in the average biofilm thickness (Figure 33).

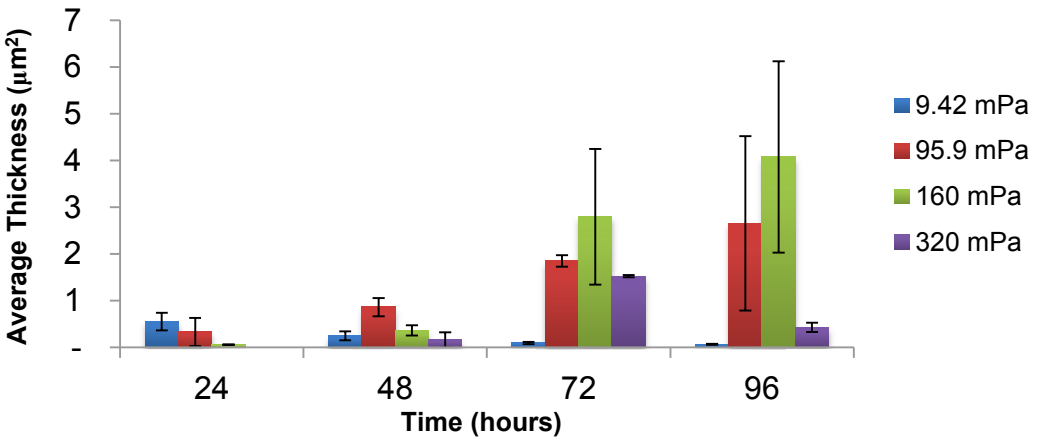

Figure 33 : The average thickness of microfluidic channel biofilms as determined by COMSTAT analysis of replicate confocal scanning laser microscopy (CLSM) Z-stacks. The biofilms were subjected to four different bulk-liquid flow velocities to exert a wide range of bulk shear stresses on the biofilms during development. Error bars indicate the standard deviation of the average thickness of duplicate biofilms, cultivated in separate microfluidic channels. Ten microscope fields, each with an area of 101,761 µm2 (318 µm × 318 µm), were chosen at random along a central transect starting from the channel inlet, and a Z-stack of images was captured in the z-direction at 0.60 µm intervals.

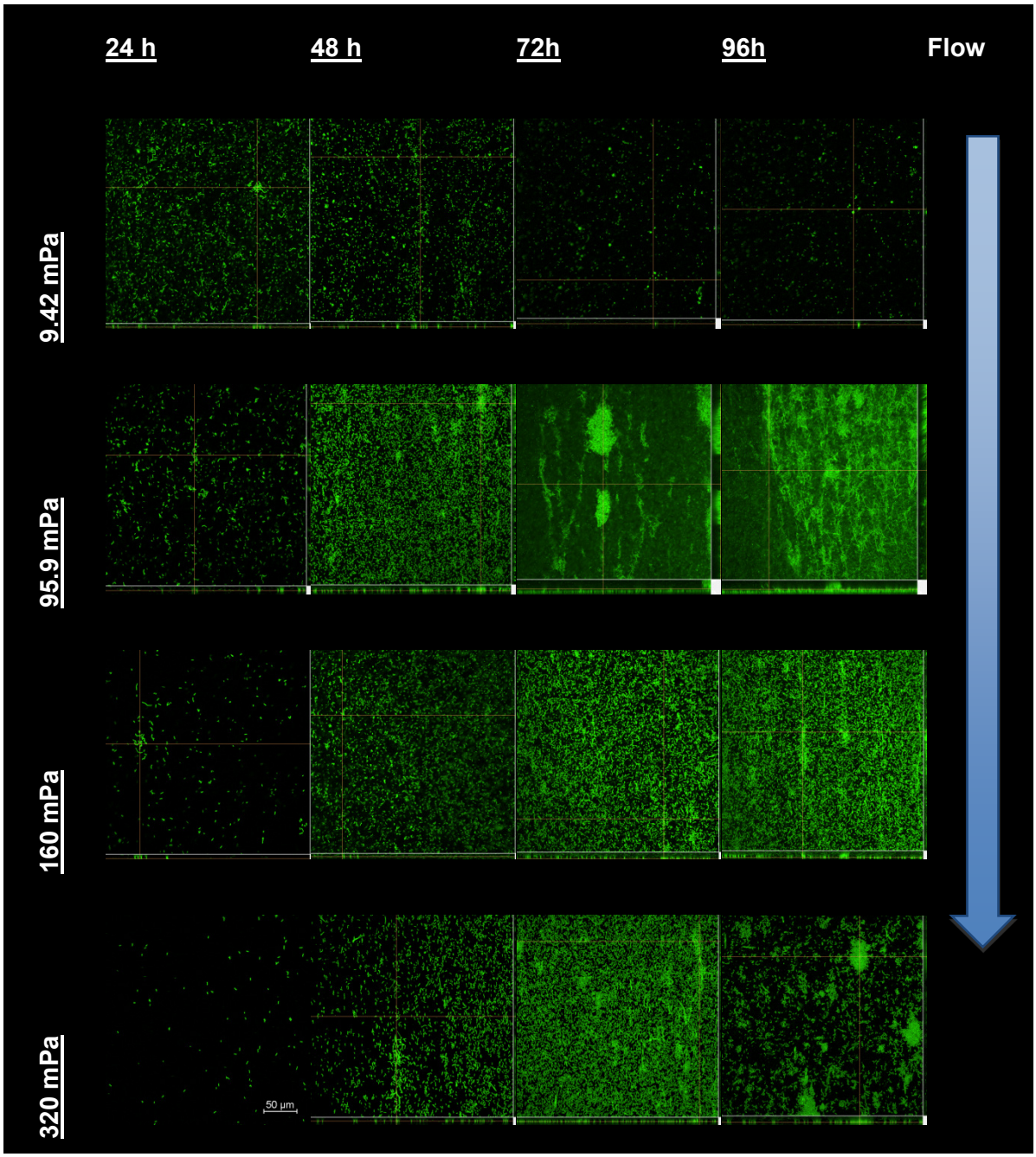

Figure 34: Representative CLSM orthogonal projections of stacks of images taken of the various biofilms at 0.6 µm depth intervals. The main part of each image consists of a single 2D slice of the biofilm (xy-direction) whereas the smaller side panels below (xz-direction) and to the right (yz-direction) indicate a digital projection of the depth of biofilm biomass from the attachment surface to the bulk-liquid interface. A scale bar indicating 50 µm is included in the bottom left image.

3.4. Biofilm Growth on Silver and Gold Layers

Future experiments will use Raman spectral imaging to monitor the growth of biofilms against a SERS surface. Since silver is typically considered an antimicrobial agent, biofilm growth was attempted against a silver layer after electroless deposition in the channel. Two similar tests were undertaken, one on silver, one on gold. In these tests, the channel was inoculated with a flow of planktonic bacteria in growth solution, followed by a flow of citrate growth solution (5 mM). As seen from Figure 35, biofilm growth occurred on both silver and gold metal layers. Evidently, the biofilm's protective matrix that surrounds bacteria is sufficient to mask the anti-microbial effects of the silver surface.

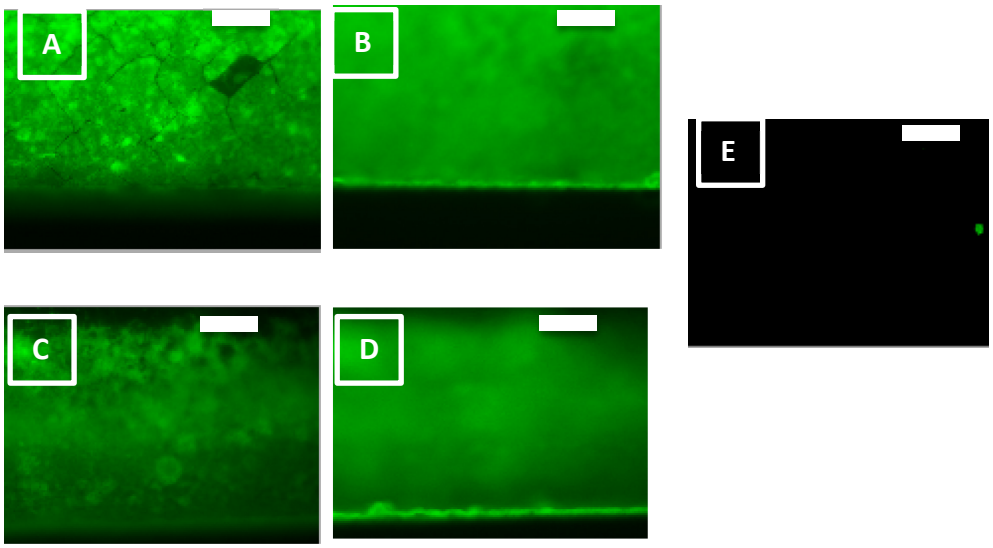

Figure 35 : Fluorescence microscope images of biofilms containing GFP bacteria in microchannels containing a silver layer. (A) Microscope image with focal point adjusted to the channel bottom shows in-focus biofilm attached to the silver layer. Small fractures and defects in the silver layer can be seen through the biofilm. (B) Same field of view shown in (A), but with focal plane moved to the glass slide. Out of focus biofilm shows that biofilm is not touching the glass and therefore the GFP signal is coming from the bottom of the channel. (C) shows a similar image to (A), but on electrolessly deposited gold. (D) Shows a similar image to (B) for the gold coated microchannel. In (B) and (D) a small amount of biofilm is in focus at the wall of the microchannel, demonstrating that some biofilm has reached the wall and climbed in the z-direction to reach the focal plan at or close to the glass slide. (E) A reference image for each channel was acquired with no GFP biofilm present, showing that the GFP bacteria are the only source of fluorescent light. Scale bars are 20 μm

.

Conclusion

In this work we presented a microfluidic-based flow-templating bioreactor maintains very accurate shear force conditions during long-term experiments, capable of localising biofilm formations to linear patterns with specified dimensions, thereby avoiding growth in the channel corners and preventing channel constrictions due to overgrowth. The effect of reactor design on the template stream dimensions was carefully considered by experiment and simulation. The width and height of the template stream could be controlled by the flow rates of the biofilm nutrient solution and the confinement solution, enabling patterns of biofilm patterns with sizes as required. Proof-of-principle experiments were conducted demonstrating growth of biofilm formations with variable widths and biofilm growth kinetics studies. Using a regular transmission light microscope, the FT-μBR can be a very useful platform for further studies into fundamental biofilm properties, such as lag times and growth rates for different bacteria under varying conditions. In addition, the ability to physically pattern biofilms with more homogeneous properties has the potential to benefit research into new biofilm-based functional materials.

Future works

Further developments could include the use new fabrication methods, such as laser cutting, to make junction holes with precise dimensions; isolation of inoculum and nutrient solution inlet channels to avoid biofilm growth upstream of the flow templating region; and the use of non-gas permeable device materials to better isolate the culture environment. In addition, the use of tracer particles such as fluorescent micro-beads can help with the characterisation of the effect of the biofilm patterns on the hydrodynamic environment in the channel can help with long-term control of biofilm formations.

Detailed of growth kinetics using the FT-μBR could study to monitor the pre-biofilm sessile bacteria population sizes in time within the template region for different conditions, such as flow rates, concentrations, surface materials and temperatures.

References

1. T. O. Peulen and K. J. Wilkinson, *Environ. Sci. Technol*., 2011, **45**, 3367-3373.
2. D. N. Hohne, J. G. Younger and M. J. Solomon, *Langmuir*, 2009, **25**, 7743-7751.
3. J. Kim, H. S. Kim, S. Han, J. Y. Lee, J. E. Oh, S. Chung and H. D. Park, *Lab Chip*, 2013, **13**, 1846-1849.
4. K. Drescher, Y. Shen, B. L. Bassler and H. A. Stone, *Proc. Natl. Acad. Sci. USA*, 2013, **110**, 4345-4350.
5. G. Wolfaardt, J. Lawrence, R. Robarts, S. Caldwell and D. Caldwell, *Appl. Environ. Microbiol.*, 1994, **60**, 434-446.
6. Y. Liu and J. H. Tay, *Water Res.,* 2002, **36**, 1653-1665.
7. F. Paquet-Mercier, N. Babaei-Aznaveh, M. Safdar and J. Greener, *Sensors*, 2013, **13**, 14714-14727.
8. J. Kim, H. Park and S. Chung, *Molecules*, 2012, **17**, 9818-9834.
9. M. Klausen , A. Heydorn , P. Ragas , L. Lambertsen , A. Aaes-Jorgensen , S. Molin and T. Tolker-Nielsen , *Mol. Microbiol.*, 2003, **48**, 1511-24.
10. H. Mikkelsen, Z. Duck, K. S. Lilley, and M. Welch, *J. Bacteriology*, 2007, **189**, 2411-2416.
11. H. Flemming and J. Wingender, *Nat. Rev. Microbiol.*, 2010, **8**, 623-633.
12. P. Lembre, C.Lorentz and P. Di Martino, *Intech.*, 2012, 371-392.
13. J. W. Costerton and Z. Lewandowski, *Annu. Rev. Microbial.,* 1995, **49**, 711-745.
14. M. E. Olson, H. Ceri, D. W. Morck, A. G. Buret, and R. R. Read, *Can. J. Vet. Res.,* 2002, **66**, 86-92.
15. M. E. Davey,and G.A. O'toole, *Microbiol. Mol. Biol. Rev.*, 2000, **64**, 847-867.
16. I. W. Sutherland, *Trends Microbiol.,* 2001, **9**, 222-227.
17. K. Ikuma, A. W. Decho and B. L. T. Lau, *Nature Education Knowledge,* 2013, **4**, 2.
18. L. Hall-Stoodley, J.W. Costerton and P. Stoodley, *Nature reviews Microbiology,* 2004, **2**, 95-108.
19. http://biotuesdays.com/2010/10/19/innovotech-targets-personalized-medicine-for-bacteria/
20. L. T. Angenent, K. Karim, M. H. Al-Dahhan, B. A. Wrenn and R. Domı´guez-Espinosa, *Trends Biotechnol.,* 2004, **22**, 477-85.
21. Q. Achton Acton , *Pseudomonas-Advances in Research and Treatment*, Scholarly Editions Atlanta, Georgia*,* 2013, 151-152.
22. K. Rabaey ,and W. Verstraete, *Trends Biotechnol.*, 2005, **23**, 291-298.
23. http://lewisdartnell.com/sparks_page.htm.
24. B. Rosche, X. Z. Li, B. Hauer, A. Schmid and K. Buehler, *Trends Biotechnol*., 2009, **27**, 636-643.
25. M. Alaraj, Z.J. Ren,and J.D Park, *J. Power Sources*, 2014, **247**, 636-642.
26. V. Sharma,and P.P. Kundu , *Enzyme . Microb. Tech.,* 2010, **47**, 179-188.

27. http://www.seminarsonly.com/mech%20&%20auto/Microbial-Fuel-Cells.php
28. P. Tabeling, *Introduction to Microfluidics*, Oxford University Press Inc., New York, 2005,1-14.
29. H. A. Stone, A. D. Stroock and A. Ajdari, *Annu. Rev. Fluid Mech*., 2004, **36**, 381-411.
30. N. Nguyen, S. T. Wereley, *Fundamentals and Applications of Microfluidics*, Artech House Inc., Norwood, MA, 2002,45, 2.
31. N. Szita1, K. Polizzi, N. Jaccard, and F. Baganz, *Curr. Opin. Biotechnol.*, 2010, **21**, 517-523.
32. N. Babaei-Aznaveh, M. Safdar, G. Wolfaardt,and J. Greener, *Lab Chip*, 2014, **14**, 2666-72.
33. B. Bhushan, *Encyclopedia of Nanotechnology, Springer*, Powell, Ohio, 2012.
34. Y. Liu,and J.H Tay, *Water Res.*, 2002, **36**, 1653-1665.
35. L. Richter, C. Stepper, A. Mak, A.Reinthaler, R. Heer, M. Kast, H. Bru¨ckl and P.Ertl, *Lab Chip*, 2007, **7**, 1723-31.
36. J. Lee, J. B. Kaplan,and W. Y. Lee, *Biomed Microdevices*, 2008, **10**, 489-498.
37. D. J. Beebe, G. A. Mensing, and G. M.Walker, *Biomed. Eng*., 2002, **4**, 261-286.
38. S. K. Sia, G. M. Whitesides, *Electrophoresis*, 2003, **24***,* 3563-3576.
39. E. L. Cussler, *Diffusion: Mass transfer in fluid systems*, Cambridge University Press, New York, 2007.
40. E. R. Chobana, L. J. Markoski, A. Wieckowski and P. J.A. Kenis, *J. power Sources*, 2004, **128**, 54-60.
41. J. L. Song, K. H. Au, K. T. Huynh and A. I. Packman , *Biotechnol. Bioeng*., 2014, **111**, 597-607.
42. E. Bester, G. M. Wolfaardt, N. Babaei-Aznaveh and J. Greener, *Int. J. Mol. Sci*., 2013, **14**, 21965-21982.
43. J. Kim, M.Hegde, S. H. Kim, T. K. Wood and A. Jayaraman, *Lab Chip*, 2012, **12**, 1157-1163.
44. L. Richter, C. Stepper, A. Mak, A. Reinthaler, R. Heer, M.Kast, H.Brückl and P.Ertl. *Lab Chip*, 2007,**7**, 1723-1731.
45. J Kim, H.S. Kim, S. Han, J.Y. Lee, J. E. Oh, S.Chung and H. D. Park, *Lab Chip*, 2013, **13**, 1846-1849.
46. S. Choi,and J. Chae, *Sens. Actuators A: Phys*., 2013, **195**, 206-212.
47. http://eol.org/data_objects/28590817.
48. D.J. Clark and O. Maaloe, *J. Mol. Biol*., 1967, **23**, 99-112.
49. Y. Xia and G. M. Whitesides, *Angew. Chem. Int. Ed.*, 1998, **37**, 550-575.
50. D. Qin, Y. Xia ,and G. M Whitesides, *Nat. protocols*, 2010, **5**, 491-502.
51. http://cnx.org/content/m25448/latest/
52. M.Schlesinger, M. Paunovic, John Wiley & Sons, *Inc*., *Hoboken, NewJersey,* 2010.
53. E. Bester, O. Kroukamp, G. M. Wolfaardt, L. Boonzaaier and S. N. Liss, *Appl. Environ. Microbiol.*, 2010, **76**, 1189-1197.
54. R. Bakke and P. Q. Olsson, *J. Microbiol. Methods*, 1986, **5**, 93-98.

55. R. Bakke, R. Kommedal and S. Kalvenes, *J. Microbiol. Methods*, 2001, **44**, 13-26.
56. S. Haruta, T. Yoshida, Y. Aoi, K. Kaneko and H. Futamata, *Microbes Environ.*, 2013, **28**, 285-294.
57. T. O. Peulen and K. J. Wilkinson*, Environ. Sci. Technol.*, 2011, **45**, 3367-3373.
58. A. Gunther and K. F. Jensenb, *Lab Chip*, 2006, **6**, 1487-1503.
59. H. A. Stone, A. D. Stroock and A. Ajdari, *Annu Rev. Fluid Mech.*, 2004, **36**, 381-411.
60. T. M. Squires,and S. R. Quake, *Rev. Mod. Phys*., 2005, **77**, 977-1026.
61. H. J. Eberl, C. Picioreanu, J. J. Heijnen,and M.C.M. Van Loosdrecht, *Chem. Eng. Sci.*, 2000, **55**, 6209-6222.
62. O. Kroukamp, R. G. Dumitrache,and G. M. Wolfaardt, Appl*. Environ. Microbiol*., *2010,* **76**, 6025-6031.
63. P.S. Stewart, *Biotechnol. Bioeng.*, 1993, **41**, 111-117.